THE ^{12}C + ^{12}C REACTION AND THE IMPACT ON NUCLEOSYNTHESIS IN MASSIVE STARS

M. PIGNATARI[1,10], R. HIRSCHI[2,3,10], M. WIESCHER[4,5], R. GALLINO[6], M. BENNETT[2,10], M. BEARD[4,5,10],
C. FRYER[7,10], F. HERWIG[5,8,10], G. ROCKEFELLER[7,10], AND F. X. TIMMES[5,9,10]
[1] Department of Physics, University of Basel, Klingelbergstrasse 82, CH-4056 Basel, Switzerland; marco.pignatari@unibas.ch
[2] Astrophysics Group, EPSAM Institute, Keele University, Keele, ST5 5BG, UK
[3] Institute for the Physics and Mathematics of the Universe, University of Tokyo, 5-1-5 Kashiwanoha, Kashiwa 277-8583, Japan
[4] Department of Physics, University of Notre Dame, Notre Dame, IN 46556, USA
[5] The Joint Institute for Nuclear Astrophysics, Notre Dame, IN 46556, USA
[6] Universita' di Torino, Torino, Via Pietro Giuria 1, I-10126 Torino, Italy
[7] Computational Physics and Methods (CCS-2), LANL, Los Alamos, NM 87545, USA
[8] Department of Physics & Astronomy, University of Victoria, Victoria, BC V8P5C2 Canada
[9] Arizona State University (ASU), School of Earth and Space Exploration (SESE), P.O. Box 871404, Tempe, AZ 85287-1404, USA
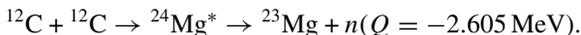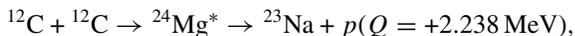
ABSTRACT

Despite much effort in the past decades, the C-burning reaction rate is uncertain by several orders of magnitude, and the relative strength between the different channels ^{12}C(^{12}C, α)^{20}Ne, ^{12}C(^{12}C, p)^{23}Na, and ^{12}C(^{12}C, n)^{23}Mg is poorly determined. Additionally, in C-burning conditions a high ^{12}C+^{12}C rate may lead to lower central C-burning temperatures and to ^{13}C(α, n)^{16}O emerging as a more dominant neutron source than ^{22}Ne(α, n)^{25}Mg, increasing significantly the s-process production. This is due to the chain ^{12}C(p, γ)^{13}N followed by ^{13}N(β+)^{13}C, where the photodisintegration reverse channel ^{13}N(γ, p)^{12}C is strongly decreasing with increasing temperature. Presented here is the impact of the ^{12}C+^{12}C reaction uncertainties on the s-process and on explosive p-process nucleosynthesis in massive stars, including also fast rotating massive stars at low metallicity. Using various ^{12}C+^{12}C rates, in particular an upper and lower rate limit of ~50,000 higher and ~20 lower than the standard rate at 5×10^8 K, five 25 $M_\odot$ stellar models are calculated. The enhanced s-process signature due to ^{13}C(α, n)^{16}O activation is considered, taking into account the impact of the uncertainty of all three C-burning reaction branches. Consequently, we show that the p-process abundances have an average production factor increased up to about a factor of eight compared with the standard case, efficiently producing the elusive Mo and Ru proton-rich isotopes. We also show that an s-process being driven by ^{13}C(α, n)^{16}O is a secondary process, even though the abundance of ^{13}C does not depend on the initial metal content. Finally, implications for the Sr-peak elements inventory in the solar system and at low metallicity are discussed.

Key words: stars: abundances – stars: evolution – stars: interiors

Online-only material: color figures

1. INTRODUCTION

During the evolution of massive stars (initial mass $\gtrsim 8\,M_\odot$), ^{12}C fusion occurs in the stellar core and, during more advanced phases, in convective shells. The lifetime of central carbon burning is governed by the balance between the energy generated by the fusion reaction and the energy lost by neutrinos (e.g., Arnett & Thielemann 1985; El Eid et al. 2004). Carbon fusion has three relevant channels:

$$^{12}\text{C} + {}^{12}\text{C} \rightarrow {}^{24}\text{Mg}^* \rightarrow {}^{20}\text{Ne} + {}^4\text{He}(Q = +4.616\,\text{MeV}),$$

$$^{12}\text{C} + {}^{12}\text{C} \rightarrow {}^{24}\text{Mg}^* \rightarrow {}^{23}\text{Na} + p(Q = +2.238\,\text{MeV}),$$

$$^{12}\text{C} + {}^{12}\text{C} \rightarrow {}^{24}\text{Mg}^* \rightarrow {}^{23}\text{Mg} + n(Q = -2.605\,\text{MeV}).$$

The first two channels have approximately the same probability, whereas the probability of the neutron channel is about two orders of magnitude lower (Dayras et al. 1977). However, it is the uncertainty of the relative strength of these channels at stellar energies (see next section for details), where no direct measurements are available, that is of particular relevance.

Despite considerable experimental efforts, the total ^{12}C+^{12}C fusion reaction rate remains uncertain at stellar temperatures.

Recent heavy ion fusion systematic studies have indicated that the fusion cross section may be hindered at low energies (Jiang et al. 2007). This would result in a lower rate than commonly used (Caughlan & Fowler 1988, hereafter CF88). On the other hand, recent low-energy experiments (Spillane et al. 2007) suggest an enhancement of the rate due to the presence of resonant structure effects at lower energies than previously considered (Gasques et al. 2005; Jiang et al. 2007; Gasques et al. 2007). This could result in a much higher ^{12}C+^{12}C fusion rate close to the Gamow peak temperature. Therefore, the present uncertainty of the ^{12}C+^{12}C rate still covers orders of magnitude at stellar temperatures.

Because both protons and α particles are products of ^{12}C+^{12}C fusion, C−burning is the first phase during massive star evolution where proton- and α-capture reactions can be efficiently activated at the same time. Leftover ^{22}Ne, from the previous convective He−burning core, efficiently captures α particles via the reaction ^{22}Ne(α, n)^{25}Mg, driving neutron-capture nucleosynthesis on the stellar material (e.g., Raiteri et al. 1991a). The ^{22}Ne(α, n)^{25}Mg reaction has been recognized as the dominant source of neutrons for the s-process in massive stars. Indeed, the reaction is active in the convective core He-burning and subsequent C-burning phases, and is responsible for the majority of the s-process species between iron and strontium observed in the solar system (Peters 1968; Lamb et al. 1977; Couch et al. 1974; Käppeler et al. 1989; Prantzos et al. 1990a; Raiteri et al.

---
[10] NuGrid collaboration.

1993; The et al. 2007; Pignatari et al. 2010). A large fraction of pre-supernova material is affected by convective carbon shell nucleosynthesis. On the other hand, material processed by C-burning in the core is usually modified and processed by later evolutionary burning phases (e.g., Woosley & Weaver 1995; Limongi et al. 2000; Rauscher et al. 2002; Woosley et al. 2002). This scenario may be modified however by uncertainties in the $^{12}C+^{12}C$ reaction rate.

The impact of the $^{12}C+^{12}C$ uncertainty in massive star simulations has been studied previously by, e.g., Gasques et al. (2007), where the consequences arising from a lower rate were considered, and by Bennett et al. (2012; hereafter Paper I), where a higher rate was used for stars of various initial masses at solar metallicity. The main results obtained in Paper I are the following: (1) For all stellar masses considered ($M =$ 15–60 $M_{\odot}$), using the upper limit $^{12}C+^{12}C$ rate (CU rate, see also the next sections) results in $^{13}C(\alpha, n)^{16}O$ becoming the predominant neutron source, compared with the established source $^{22}Ne(\alpha, n)^{25}Mg$ and increases the s-process stellar yields by up to $\sim$2 orders of magnitude. (2) When an intermediate rate (CI, Paper I) is used, s-process-rich material from the C core is only ejected for the 20 $M_{\odot}$ mass. For this one case, the stellar model shows similar results to that of the 20 $M_{\odot}$ star using the CU rate, whereas all other models show results comparable to the standard case using the CF88 $^{12}C+^{12}C$ rate. (3) For all of the masses considered, the lifetime of central C-burning increases with increasing the $^{12}C+^{12}C$ rate. The density and temperature of C-burning decrease with increasing $^{12}C+^{12}C$ rate. No significant variation trends are observed for more advanced phases. (4) Point (1) suggests that the CU rate is likely too high, since it would be hard to reconcile the predicted yields with observations, such as the solar s-process distribution.

In this paper, for one 25 $M_{\odot}$ star we consider the complete range of the present $^{12}C+^{12}C$ uncertainty, in agreement with Gasques et al. (2007) and Paper I. We discuss the importance of the rate uncertainty on the s-process and on explosive p-process yields, which are driven by photodisintegration on s-process-rich material during core collapse (e.g., Arnould & Goriely 2003, and reference therein). We consider the implications for the s-process arising from the large uncertainty regarding the relative strengths of the three carbon fusion channels, an effect that was not included in the two works mentioned above. The impact of the neutron source $^{13}C(\alpha, n)^{16}O$ is also considered for non-rotating and fast-rotating massive stars, with halo metallicities. Finally, the production of unstable long-lived species ^{26}Al and ^{60}Fe in the pre-explosive phase is revised within the $^{12}C+^{12}C$ uncertainty (e.g., Arnett & Truran 1969; Timmes et al. 1995b; Limongi & Chieffi 2006).

The paper is organized as follows. The present uncertainty of the $^{12}C+^{12}C$ reaction rate and its nucleosynthesis channels is discussed in Section 2. Presented in Section 3 are the main features of the stellar models used in this work. In Sections 4 and 5, the s-process in the convective He-burning core and in C-burning conditions is described. The impact on nucleosynthesis of different $^{12}C+^{12}C$ channels is discussed in Sections 6 and 7. The p-process nucleosynthesis is analyzed in Section 8, and in Section 9 the importance of the $^{12}C+^{12}C$ uncertainty is explored at low metallicity, for non-rotating and fast-rotating stars. Finally, conclusions are presented in Section 10.

2. ($^{12}C + ^{12}C$) REACTION

The $^{12}C+^{12}C$ reaction is one of the most studied heavy ion fusion processes. Considerable effort has been expended over the last decades on the measurement of the $^{12}C+^{12}C$ fusion cross section at very low energies (Patterson et al. 1969; Mazarakis & Stephens 1973; High & Čujec 1977; Kettner et al. 1980; Becker et al. 1981; Rosales et al. 2003).

Despite these dedicated efforts, the low-energy reaction rate still carries considerable uncertainties due to pronounced resonance structures that are thought to be associated with molecular $^{12}C+^{12}C$ configurations in the $^{24}Mg^{*}$ system (Bromley et al. 1960). While this observation is significant for the understanding and interpretation of nuclear structure configurations (Freer 2007), it may also have a significant impact on the actual reaction rate of $^{12}C+^{12}C$ fusion in stellar burning environments. The stellar reaction rate depends critically on the S-factor in the stellar energy regime, which so far has been inaccessible to laboratory studies. The low, sub-picobarn cross sections and the substantial beam-induced background events on target impurities make the identification and measurement of the reaction products difficult (Strieder 2010), and generally the expanding of the measurement of the $^{12}C+^{12}C$ fusion cross section to very low energies (Zickefoose et al. 2011). In particular, the resonance configurations are characterized by pronounced structures associated with the $^{24}Mg^{*}$ compound nucleus in the corresponding excitation range, and should be strongly populated in the fusion process except for the hindrance by Coulomb and orbital momentum barrier. The experimental data indicate that these resonances have relatively narrow total widths, $\Gamma \approx 100$ keV. Since these resonance levels are highly unbound with respect to α and proton decay, the α cluster and proton single-particle component in the wave function is relatively small, corresponding to spectroscopic factors of $\leqslant 0.01$ for both decay channels. This is also reflected in the results of elastic $^{20}Ne(\alpha, \alpha)$ (Abegg & Davis 1991; Davis 1981) and $^{23}Na(p, p)$ (Vanhoy et al. 1987) scattering experiments, which indicate no pronounced α or single-particle structure in this particular excitation range of ^{24}Mg. Despite considerable theoretical effort, the exact nature and structure of these molecular resonance levels is not fully understood and low-energy reaction cross section extrapolations are mostly based on averaging the cross section over the resonance structure (Fowler et al. 1975). A recent potential model analysis of the fusion cross section (Gasques et al. 2005) was based on the Sao Paulo model and resulted in a theoretical prediction of the cross section, describing well the experimental data and allowing extrapolation to lower energies. The results were in good agreement with the previous phenomenological approach by Fowler et al. (1975).

More recently, however, it has been argued on the basis of heavy ion fusion systematics that the low-energy cross section of fusion reactions declines faster with decreasing energy than projected by the potential model. This has been modeled by introducing an additional term in the potential that is related to the incompressibility of nuclear matter (Mişicu & Esbensen 2006). This term translates into a hindrance effect for the fusion process, suggesting a significant reduction of the overall cross section toward low energies. This effect has been confirmed by a number of low-energy fusion reactions with positive Q-values (Jiang et al. 2008), and it is argued that the hindrance effect may also reduce the low-energy S-factor of the $^{12}C+^{12}C$ fusion process significantly (Jiang et al. 2007). The impact of such a reduction on a number of stellar burning scenarios was discussed in a previous study (Gasques et al. 2007).

On the other hand, recent low-energy experiments (Spillane et al. 2007) indicate the existence of strong molecular resonances at even lower energies than previously considered (Gasques et al.

2005, 2007; Jiang et al. 2007). These resonances may contribute significantly to the low-energy cross section and enhance the reaction rate substantially. One pronounced ^{12}C+^{12}C resonance structure has been reported in both the proton and the α channel, at E_{cm} = 2.138 MeV (Spillane et al. 2007), and another resonance at $E_{cm} \approx 1.5$ MeV has been projected on the basis of a theoretical evaluation of recent ^{12}C+^{12}C scattering data, which seems to indicate the existence of a pronounced resonance also at 1.5 MeV (Perez-Torres et al. 2006). The total strength of the resonance at 2.14 MeV is projected to be $\omega\gamma \leqslant 0.13$ MeV. This is remarkably large and translates into a pronounced ^{12}C+^{12}C cluster configuration with a spectroscopic factor of $C^2S_{12C} \approx 1$.[11] Adopting this value for the resonance at 1.5 MeV, we obtain an upper limit for the total resonance strength of $\omega\gamma \leqslant 0.01$ μeV. A thorough search was performed to identify this resonance at low ^{12}C+^{12}C in the proton channel ^{12}C(^{12}C, p)^{23}Na. Unfortunately, the measurements were affected by the beam-induced proton background from the resonant ^{12}C(d, p)^{13}C reaction, triggered by deuteron recoils from elastic ^{12}C beam scattering on low-level deuteron impurities in the ^{12}C target (Zickefoose et al. 2011). The yield of this two-step background process presently sets the upper limit for the resonance strength of ^{12}C(^{12}C, p)^{23}Na below E_{cm} = 2.5 MeV. Recent unpublished experimental data with ultrapure ^{12}C targets and greatly reduced deuterium contamination did not show any indications for lower energy resonances (Zickefoose 2011). While this background also affects the proposed strong ^{12}C(^{12}C, p)^{23}Na resonance at E_{cm} = 2.138 MeV (Spillane et al. 2007), the possibility of a ^{12}C+^{12}C cluster resonance reflected in the ^{12}C(^{12}C, α)^{20}Ne reaction channel cannot be excluded, since the α channel was not observed in this particular experiment.

Complementary information may come from α-scattering, α-capture and α-emission data because a ^{12}C cluster configuration may also show an enhanced α-cluster signature. Indeed, the ^{20}Ne(α, α_0) elastic scattering data by Abegg & Davis (1991) indicate a number of strong natural parity states in the excitation range of interest. No radiative capture data are available for this energy range (Endt 1990), but several levels have been observed in the ^{23}Na(p, α)^{20}Ne reaction. Overall, the complementary information is sparse, since not many experiments have systematically probed the level structure of ^{24}Mg above 15 MeV.

Evaluating the available information, most notable are the two states at 15.44 MeV ($J^\pi = 0^+$, $T = 2$) and 16.07 MeV ($J^\pi = 6^+$, $T = 0$), which match the energies of the two postulated low-energy resonances in the ^{12}C+^{12}C channel at E_{cm} = 1.5 MeV (Perez-Torres et al. 2006) and E_{cm} = 2.14 MeV (Spillane et al. 2007). The 15.44 MeV level has been observed in a number of scattering and reaction studies, and was identified as a $T = 2$ isospin state. The total width, as well as the proton and α partial widths, is known or can be deduced from the available experimental information such as ^{23}Na(p, α) and ^{23}Na(p, p) (McDonald et al. 1978; Endt 1990).

The critical parameters that need to be defined in order to determine the resonance strengths in the fusion process are the ^{12}C partial widths for these levels. The level at 16.07 MeV has only been observed in high spin transfer reactions (Ford et al. 1974),

and the proton and α partial widths cannot be directly evaluated. If these two levels correspond to the observed ^{12}C+^{12}C resonance states, it would require a pronounced ^{12}C+^{12}C cluster configuration for both levels. Some information can be extracted on the basis of this assumption. The population of a pure $T = 2$ level is isospin forbidden; it is only possible with strong isospin mixing. In the case of the 15.44 MeV state, the existence of isospin mixing is confirmed by the observation of the α emission (McDonald et al. 1978) and the α decay of this level (McGrath et al. 1970). The isospin mixing can actually be deduced from the strength of the α decay branch to be ≈ 0.01, adopting a pronounced ^{20}Ne+^{4}He cluster configuration. This result is relatively insensitive to the choice of the radius of the system. On the other hand, a pronounced ^{12}C+^{12}C cluster structure is associated with a large interaction radius of $R = 8.5$ fm. The ^{12}C partial width of the 16.07 MeV 6^+ state is limited by the $\ell = 6$ orbital momentum barrier. This level has not been observed in any of the proton or α induced scattering or reaction processes. The available information about the proton and α partial widths relies on the recent measurement of the resonance strengths for both branches in the ^{12}C+^{12}C fusion reaction (Spillane et al. 2007). The measured resonance strengths are consistent with the large interaction radius of $R = 8.5$ fm, anticipated for a cluster configuration of this level.

On the basis of these considerations, we have re-evaluated the reaction rate for the ^{12}C+^{12}C fusion reaction as well as the rates for the two most important reaction channels, ^{12}C(^{12}C, α)^{20}Ne and ^{12}C(^{12}C, p)^{23}Na. While these two channels are responsible for the energy production by carbon fusion and for the production of seed material for the next Ne-burning stage, the third channel, ^{12}C(^{12}C, n)^{23}Mg, may contribute as the neutron source for s-process nucleosynthesis at higher temperature environments. This possibility will be discussed in Section 7. Figure 1 shows the total ^{12}C+^{12}C rate with the evaluated uncertainties. Note that in the figure the neutron channel is neglected; the reaction is endothermic with a negative Q-value of -2.6 MeV and contributes less than 4% at higher energies to the total cross section. The "lower limit" (CL) of the rate corresponds to the one suggested on the basis of an extrapolation of the averaged data, using a potential model approach that includes a hindrance term for low-energy fusion processes (Gasques et al. 2007). The recommended rate is based on the classical extrapolation of the averaged S-factor data using a standard potential model (Gasques et al. 2005) plus the contribution of a single resonance observed at E_{cm} = 2.13 MeV, and is quite similar to the standard CF88 rate. The "upper limit" (CU) includes an additional term resulting from a possible strong ^{12}C+^{12}C cluster resonance at E_{cm} = 1.5 MeV. The resonance parameters have been estimated as outlined above. The total rates are listed in Table 1.

3. STELLAR MODELS

In order to assess the importance of the ^{12}C+^{12}C rate for the s-process in massive stars, five 25 $M_\odot$ stellar models were calculated using different ^{12}C+^{12}C rates. Apart from the ^{12}C+^{12}C rate, all of the models were calculated with identical input physics, and were therefore identical at the end of He-burning. Calculations were performed using the Geneva stellar evolution code (GENEC), described in Hirschi et al. (2004) and Eggenberger et al. (2008). We recall here the main input physics used.

The initial metal content was $Z = 0.01$, where the solar abundances were given by Anders & Grevesse (1989) for

---

[11] During a nuclear reaction, a new nucleus is formed with the nucleons occupying a given configuration (which also defines spin and parity). There are two ways of measuring the likelihood of a configuration: one where the isospin of the nucleons is neglected and another where it is included. C^2S_{12C} is the notation for the ^{12}C+^{12}C spectroscopic factor, including the isospins of the nucleons. The fact that it is nearly 1 means that this is a very likely configuration.
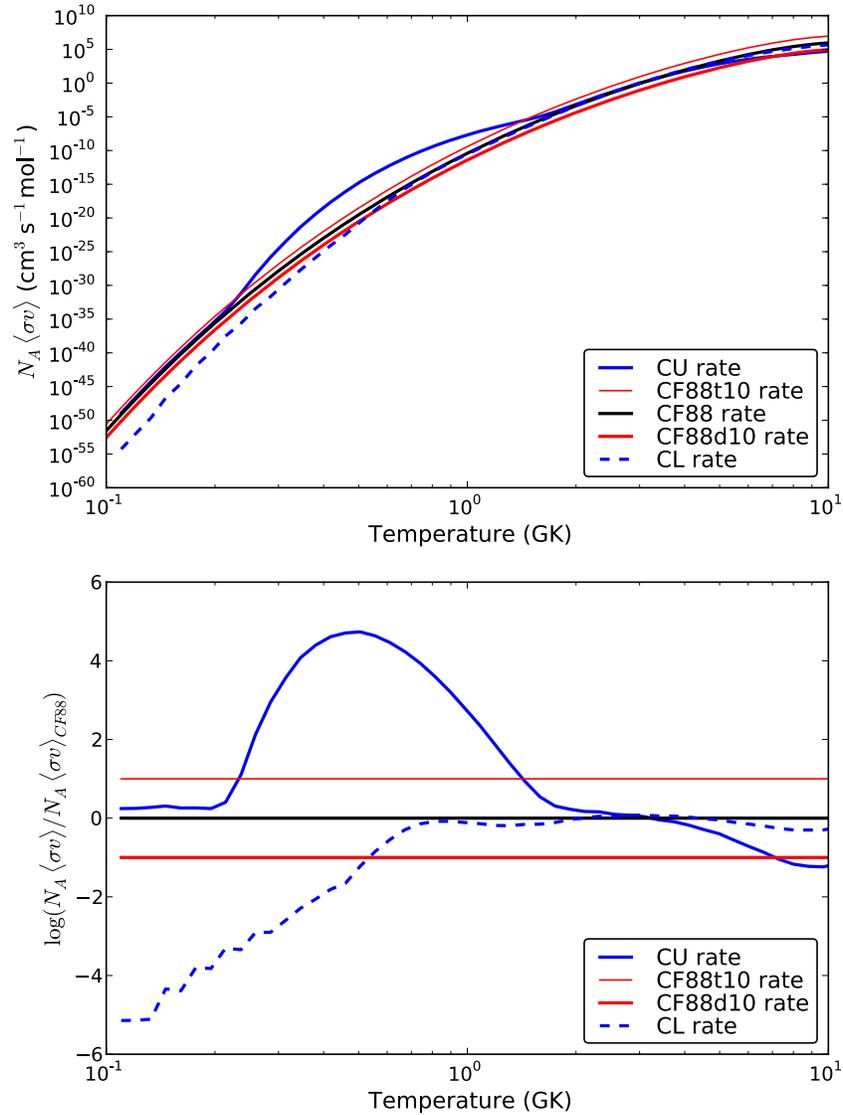
Figure 1. Top panel: the ^{12}C+^{12}C reaction rate used in this study. The CU and CF88 rates are the same as used in Paper I (Bennett et al. 2012). Bottom panel: the rates are shown normalized to the standard case (CF88).

(A color version of this figure is available in the online journal.)

the total elemental abundances, and by Lodders (2003) for the relative isotopic abundances. The corresponding OPAL opacity tables are taken from Rogers et al. (1996), except at low temperatures, where instead opacities from Ferguson et al. (2005) were used. The convective boundaries were defined according to the Schwarzschild criterion. Overshooting was applied for core H- and core He-burning only, using an overshooting parameter, $\alpha = 0.2$ H_P, as in Maeder (1992). Effects from rotation and magnetic fields were not included in the calculation, but this does not detract from the main focus of the present investigation. For $\log T_{\rm eff} > 3.9$, O-type star mass-loss rates were adopted from Vink et al. (2001), and from de Jager et al. (1988) otherwise. With a few exceptions, reaction rates were taken from the NACRE compilation (Angulo et al. 1999). For temperatures below 0.1 GK, the ^{14}N$(p, \gamma)^{15}$O rate is taken from Mukhamedzhanov et al. (2003). Above 0.1 GK, the lower limit NACRE rate was used. This combined rate is very similar to the more recent LUNA rate (Imbriani et al. 2005), which is used in the post-processing at relevant temperatures. The 3α rate adopted is from Fynbo et al. (2005),

and the ^{12}C$(\alpha, \gamma)^{16}$O rate from Kunz et al. (2002). For the ^{22}Ne$(\alpha, n)^{25}$Mg reaction, we used the rate of Jaeger et al. (2001) for temperatures of 1 GK and below. The NACRE rate was used for higher temperatures. The ^{22}Ne$(\alpha, n)^{25}$Mg rate competes with ^{22}Ne$(\alpha, \gamma)^{26}$Mg, where the NACRE rate is used.

In Figure 2, we present the Kippenhahn evolution diagram for the five stellar models, where the ^{12}C+^{12}C rate used in the calculations are, respectively, (1) the upper limit provided in Section 2 (M25CU model, upper left panel), (2) the CF88 rate multiplied by a factor of 10 (M25CF88t10 model, upper right panel), (3) the CF88 rate (M25CF88 model, central panel), (4) the CF88 rate divided by a factor of 10 (M25CF88d10 model, lower left panel), and (5) the lower limit provided in Section 2 (M25CL model, lower right panel). The rates used for the different cases are shown in Figure 1.

All models were evolved beyond the end of central O-burning. The central temperature and density evolution are shown in Figure 3. As mentioned, the evolutionary curve in Figure 3 is the same for all the models until central He exhaustion. Models calculated using the higher ^{12}C+^{12}C rates generally

Table 1
Recommended, Upper Limit (CU) and Lower Limit Rate (CL) is Given
for the ^{12}C+^{12}C Fusion Reaction

T9	Total Rate		
	Recomm.	Lower Limit	Upper Limit
1.00E−01	4.99E−52	2.25E−58	4.99E−52
1.10E−01	1.30E−49	5.32E−55	1.30E−49
1.21E−01	2.95E−47	1.21E−52	2.95E−47
1.33E−01	5.66E−45	2.33E−50	5.66E−45
1.46E−01	8.78E−43	1.97E−47	8.78E−43
1.61E−01	1.21E−40	2.73E−45	1.21E−40
1.77E−01	1.37E−38	1.19E−42	1.37E−38
1.95E−01	1.39E−36	1.21E−40	1.41E−36
2.14E−01	1.17E−34	3.07E−38	1.57E−34
2.36E−01	8.90E−33	2.34E−36	6.46E−32
2.59E−01	5.69E−31	3.74E−34	4.04E−29
2.85E−01	3.49E−29	2.17E−32	1.53E−26
3.14E−01	2.08E−27	2.32E−30	3.38E−24
3.45E−01	1.34E−25	1.95E−28	4.55E−22
3.80E−01	8.12E−24	1.35E−26	3.85E−20
4.18E−01	3.98E−22	8.15E−25	2.16E−18
4.60E−01	1.47E−20	3.63E−23	8.31E−17
5.05E−01	3.98E−19	2.48E−21	2.25E−15
5.56E−01	8.35E−18	1.48E−19	4.47E−14
6.12E−01	1.42E−16	6.73E−18	6.68E−13
6.73E−01	2.06E−15	2.33E−16	7.68E−12
7.40E−01	2.86E−14	5.75E−15	7.01E−11
8.14E−01	3.88E−13	1.08E−13	5.16E−10
8.95E−01	5.04E−12	1.58E−12	3.13E−09
9.85E−01	5.93E−11	2.00E−11	1.59E−08
1.08E+00	6.72E−10	2.12E−10	6.87E−08
1.19E+00	6.84E−09	2.24E−09	2.63E−07
1.31E+00	6.53E−08	2.32E−08	9.02E−07
1.44E+00	5.85E−07	2.35E−07	3.01E−06
1.59E+00	4.93E−06	2.27E−06	1.12E−05
1.75E+00	3.88E−05	2.05E−05	5.37E−05
1.92E+00	2.85E−04	1.71E−04	3.17E−04
2.11E+00	1.83E−03	1.30E−03	1.89E−03
2.32E+00	1.16E−02	9.08E−03	1.18E−02
2.56E+00	6.44E−02	5.69E−02	6.46E−02
2.81E+00	3.29E−01	3.26E−01	3.30E−01
3.09E+00	1.56E+00	1.71E+00	1.56E+00
3.40E+00	6.25E+00	7.83E+00	6.25E+00
3.74E+00	2.52E+01	3.50E+01	2.52E+01
4.11E+00	8.48E+01	1.36E+02	8.48E+01
4.53E+00	2.60E+02	4.90E+02	2.60E+02
4.98E+00	7.32E+02	1.64E+03	7.32E+02
5.48E+00	1.66E+03	4.73E+03	1.66E+03
6.02E+00	3.45E+03	1.27E+04	3.45E+03
6.63E+00	6.78E+03	3.18E+04	6.78E+03
7.29E+00	1.12E+04	6.79E+04	1.12E+04
8.02E+00	1.83E+04	1.36E+05	1.83E+04
8.82E+00	3.06E+04	2.57E+05	3.06E+04
9.70E+00	4.74E+04	4.13E+05	4.74E+04
1.07E+01	7.73E+04	6.27E+05	7.73E+04

Table 2
Indicative Stellar Structure Properties for All Models

Model	$M_\alpha^{75\%}$ ($M_\odot$)	M_{CO} ($M_\odot$)	M_{final} ($M_\odot$)	CC($M_\odot$) ($M_\odot$)	T_c (GK)	ρ_c (g cm^{-3})	Shells
M25CF88d10	9.354	6.205	14.370	Radiative	0.894	2.129E+5	1
M25CL	9.354	6.206	14.369	Radiative	0.729	8.192E+4	1
M25CF88	9.169	6.347	14.710	Radiative	0.728	8.020E+4	1
M25CF88t10	9.331	6.322	13.791	Radiative	0.710	6.083E+4	2
M25CU	9.275	6.550	13.780	4.12	0.559	1.544E+4	1

Notes. For each of the stellar models presented in this work (25 $M_\odot$, $Z = 0.01$, for different ^{12}C+^{12}C rates, Column 1), the following data are provided: helium core mass ($M_\alpha^{75\%}$, i.e., giving the mass coordinate above which the He abundance drops below 75%, Column 2); CO core mass (M_{CO}, Column 3); final total mass (M_{final}, Column 4); size convective carbon core (CC($M_\odot$), Column 5); ignition temperature and density of core C-burning (T_c and ρ_c, Columns 6 and 7), respectively; number of convective C-burning shell episodes (Column 8).

Table 3
Stellar Lifetimes for Different Burning Stages in All Models

Model	τ_H	τ_{He}	τ_C	τ_{Ne}	τ_O	τ_{Si}	τ_{Total}
M25CF88d10	6.631E+6	6.213E+5	2.248E+1	0.148	0.208	0.007	7.380E+6
M25CL	6.631E+6	6.213E+5	1.726E+2	0.823	0.212	0.011	7.380E+6
M25CF88	6.631E+6	6.213E+5	1.750E+2	0.498	0.301	0.007	7.380E+6
M25CF88t10	6.631E+6	6.213E+5	4.256E+3	0.126	0.133	0.015	7.380E+6
M25CU	6.631E+6	6.213E+5	2.152E+4	0.406	0.374	0.023	7.399E+6

Notes. For each of the stellar models presented in this work (25 $M_\odot$, $Z = 0.01$, different ^{12}C+^{12}C rates, see Column 1), the lifetimes of all core burning stages and total lifetime of the star are given (in years): H-burning (τ_H, Column 2); He-burning (τ_{He}, Column 3); C-burning (τ_C, Column 4); Ne-burning (τ_{Ne}, Column 5); O-burning (τ_O, Column 6); Si-burning (τ_{Si}, Column 7), and total lifetime (τ_{Total}, Column 8). Note that all the models stop before the end of central Si-burning.

^{12}C+^{12}C rate explored in this work is larger than in Paper I, including the possibility of a rate lower than CF88. At $T \sim$ 0.7–0.8 GK, the CL rate varies from the CF88 rate by less than a factor of 10. However, there is a factor of 10 difference between CF88d10 and CF88 over the same temperature range (Figure 1). Therefore, because the CL rate rapidly increases with temperature, CF88d10 is actually the lowest carbon fusion rate we consider during central C-burning conditions. Note that the CF88d10 and CF88t10 rates are given by applying a temperature invariant correction factor to the CF88 rate over the entire temperature range. Though such constant variation is unlikely, the present models calculated with these rates are still useful as a guide, and can provide qualitative insights about the impact of the ^{12}C+^{12}C rate on stellar evolution, including later stages.

The time elapsed between He exhaustion and core C-burning activation decreases with increasing ^{12}C+^{12}C rate. However, the early C ignition is compensated by a longer core burning phase (see Figure 6 and Table 3). In Figures 4–6, the central temperature and density at C ignition and C-burning lifetimes[12] are compared. The trend observed in Paper I is also confirmed for ^{12}C+^{12}C rates lower than CF88: the temperature and density of central C ignition decreases with increasing carbon fusion rate, whereas the C-burning lifetime shows the opposite behavior. The M25CL and M25CF88 models show similar conditions for

show the signature of central C ignition at lower temperature and density conditions (upward kink in the curve in the range $\log(\rho_c) = 4$–6 g cm^{-3}). After central C-burning, no significant variations may be noticed in the T_c–ρ_c diagram in the following evolutionary phases (see below for more details), as already noted in Paper I. The main parameters of the stellar models presented in Figure 2 and 3 are summarized in Tables 2 and 3. Similar data are provided for a grid of masses and at solar metallicity in Paper I, which is similar to the case discussed here at lower metallicity. However, the range of

---

[12] The central C-burning lifetime is calculated as follows: The C fusion is assumed to start once central ^{12}C from the He core ashes is decreased by 3%, and is assumed to finish once the central ^{12}C mass fraction is less than 0.001.
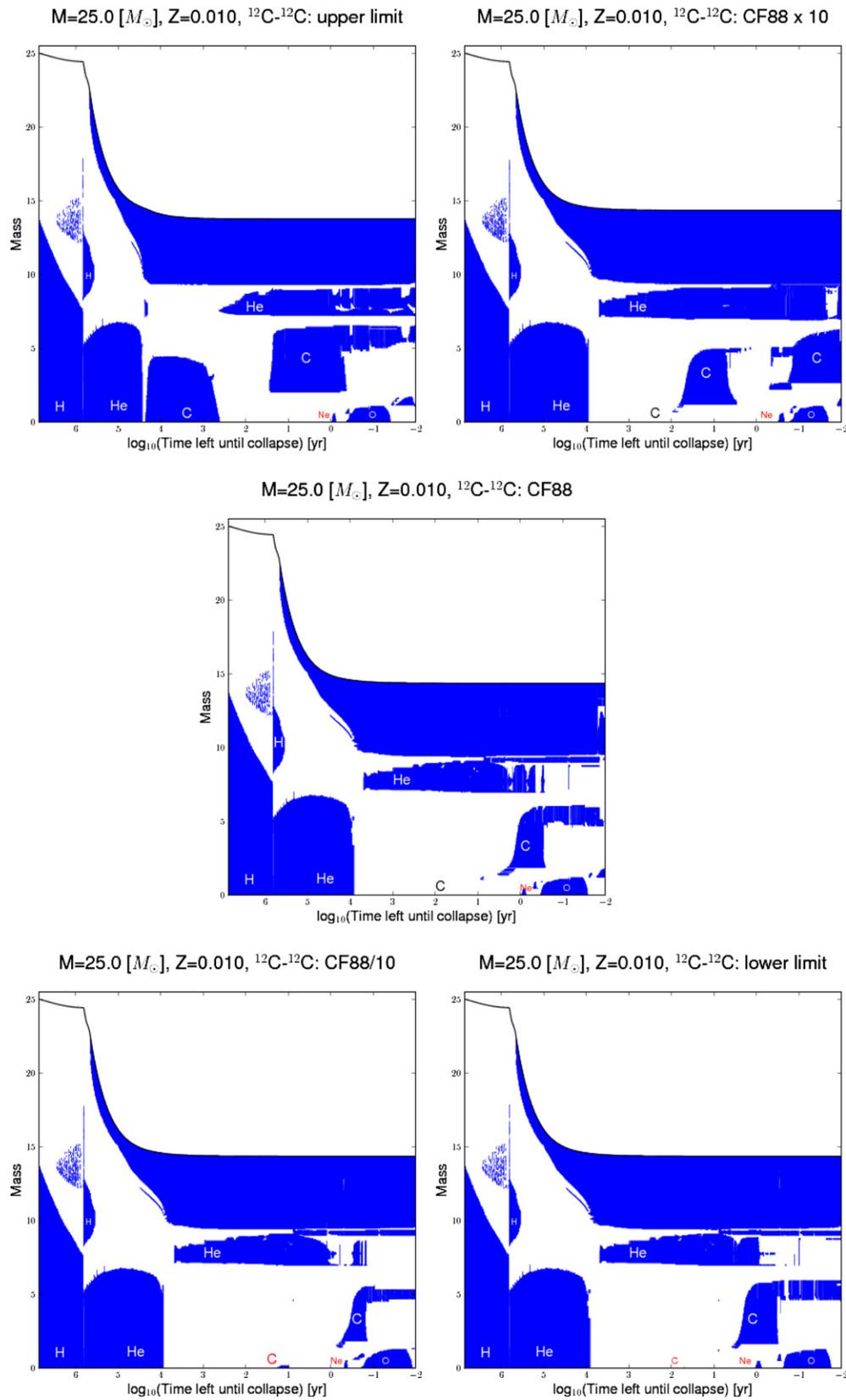
Figure 2. Kippenhahn diagram is provided for five stellar models of a 25 $M_\odot$ star, and $Z = 0.01$, calculated using different ^{12}C + ^{12}C rates (see the text for more details): the upper limit rate (CU, upper left panel), the Caughlan & Fowler (1988) rate (CF88, central panel), multiplied and divided by a factor of 10 (CF88t10 and CF88d10, upper right and lower left panels, respectively), and the lower limit rate (CL, lower right panel).

(A color version of this figure is available in the online journal.)
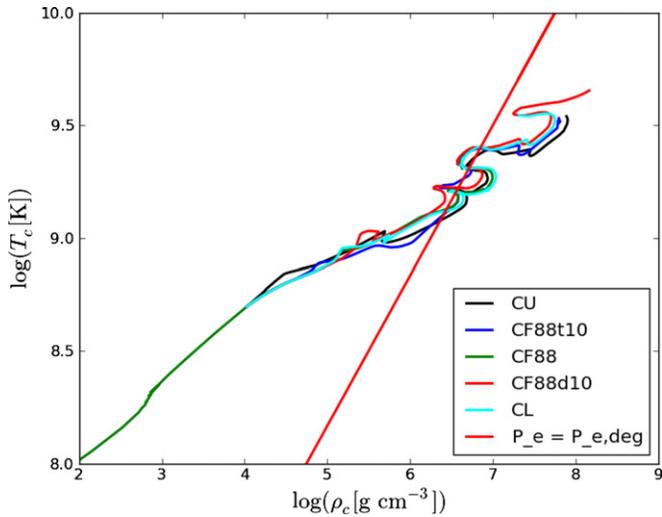
Figure 3. Evolution of central temperature versus central density for the models considered in this work. The red straight line identifies the limit between a non-degenerate and a degenerate electron gas, $P_{gas} = P_{e,deg}$.
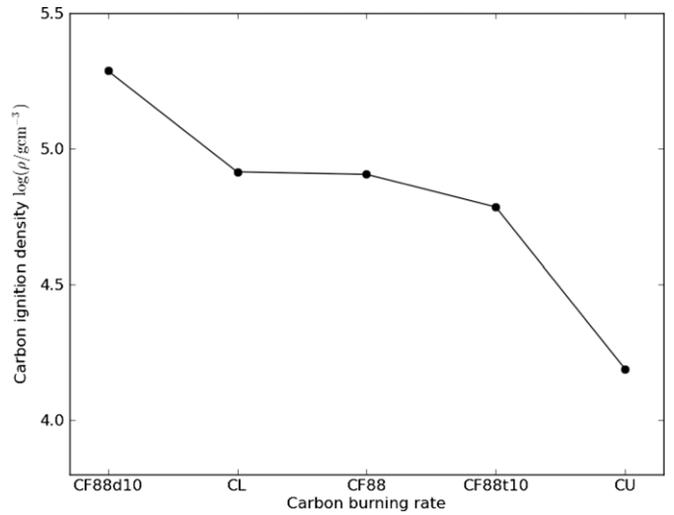
(A color version of this figure is available in the online journal.)
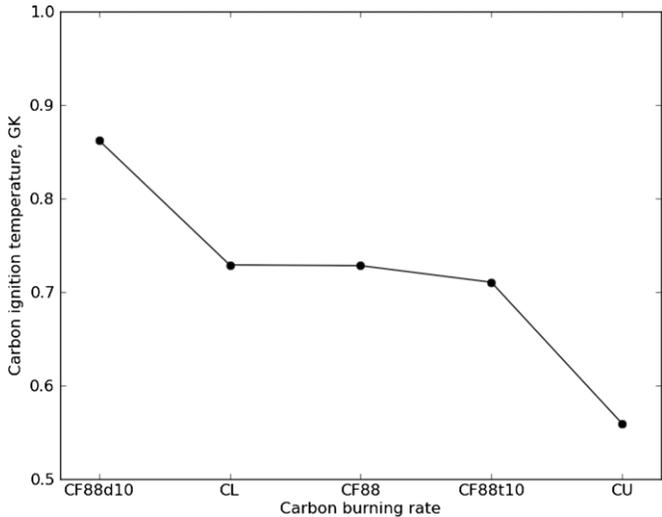
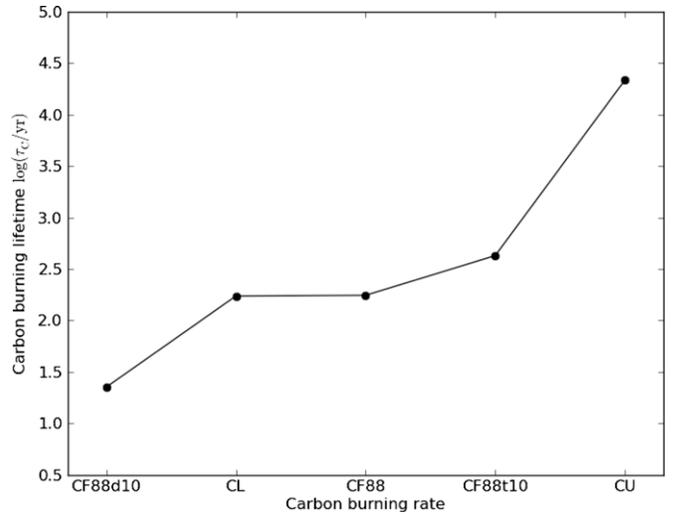**Figure 4.** Central carbon ignition temperature is shown for each stellar model, according to the ^{12}C + ^{12}C rate used. Note that the case CF88d10 shows a central C ignition at higher temperature than the case CL. This is expected, since the difference between the standard rate and the CL rate drops quickly below a factor of 10 with increasing temperature (see Figure 1).

Figure 5. As Figure 4, but for the central density.

Figure 6. As Figure 4, but for core C-burning lifetimes.

central C-burning. Indeed, at the point where central carbon ignition occurs in these models, the CL rate and the CF88 rate are quite similar, despite the fact that for lower temperatures the CL rate drops quickly compared with the standard rate. On the other hand, the M25CF88d10 and M25CF88t10 models show significantly different behaviors; reducing the ^{12}C+^{12}C rate has a larger impact compared with the CF88 case. Finally, because of the high upper limit, the M25CU model (which is about 50,000 larger than the CF88 rate, Figure 1) shows a large effect in the stellar conditions (see Tables 2 and 3), in agreement with calculations presented in Paper I.

Note that the behavior of C-burning temperature with the ^{12}C+^{12}C rate can simply be derived analytically, if we consider the temperature dependence of the C-burning rate, where $\lambda_{^{12}C^{12}C} \propto T9^{29}$ (where T9 is temperature in GK units; see Woosley et al. 2002). Indeed, if we simply consider that the amount of energy required for the stellar structure is the same, regardless of the C-burning rate, we obtain for the upper

limit a burning temperature of T9 = 0.50, and for the model M25CF88d10 T9 = 0.79. These values are only about 10% lower than the activation temperatures shown in Table 2. Such small differences are likely due to minor effects considered in the full stellar model, as for instance the neutrino feedback.

Figure 2 shows that carbon core burning is radiative for the models M25CL, M25CF88, and M25CF88t10. For the lowest rate, CF88d10, core C-burning induces a tiny convective core. The CU case, on the other hand, shows an extended convective core (up to 4.12 $M_\odot$ in size). Generally, the standard 25 $M_\odot$ model is close to the lower mass limit for radiative core carbon burning, which is around 22 $M_\odot$ (Hirschi et al. 2004). Core C-burning becomes convective once the energy produced by ^{12}C+^{12}C is higher than the energy lost by neutrinos (El Eid et al. 2004). In the CF88d10 case, the lower rate leads to a delayed C ignition at higher temperatures, where the energy generation slightly overtakes the neutrino losses. In the M25CU model, the formation of an extended convective core is due to the early activation of C-burning, where the lower temperature makes the neutrino energy loss much less efficient (Itoh et al. 1996; see also discussion in Paper I).

After central carbon exhaustion, C-burning develops in outer convective shells. Models M25CF88d10, M25CL, M25CF88,

and M25CU show one extended convective shell, whereas M25CF88t10 develops two convective shells. In this last case, the first convective shell overlaps with the second and final convective shell by about 2/3 of its total extent. In a similar way, the M25CU model shows a similar overlap between the central convective C core and the subsequent convective C shell. Such overlap has a strong impact on the composition of the final stellar ejecta. Looking at Table 3, we can see that contrary to carbon burning, all stellar models are quite similar during the subsequent burning stages (neon and oxygen burning stages; see also Paper I).

As mentioned before, the ^{12}C+^{12}C rate is the only reaction relevant for energy generation tested in this work. Note however that the uncertainty of other reactions such as ^{12}C(α, γ)^{16}O (e.g., Imbriani et al. 2001; El Eid et al. 2004, 2009; Woosley et al. 2002) or ^{16}O+^{16}O may affect stellar structure. In particular, the ^{12}C(α, γ)^{16}O affects the amount of ^{12}C left after He-burning and therefore the ensuing C-burning and Ne-burning stages. In principle, using a different ^{12}C(α, γ)^{16}O rate could affect the results discussed in the following sections. However, after having explored the impact of the ^{12}C + ^{12}C rate for stars of different masses (and therefore with different ^{12}C and ^{16}O composition at the onset of central C ignition) in Paper I, we believe that our present results are robust and cannot be significantly changed by using different ^{12}C(α, γ)^{16}O rates.

Stellar physics uncertainties (mixing-length theory approximations, prescriptions adopted for convective boundary mixing, mass loss, impact of rotation, and magnetic field; see e.g. Limongi et al. 2000; Woosley et al. 2002; Meynet et al. 2006) may also affect stellar models. Furthermore, multi-dimensional simulations for advanced stages of massive stars showed several features that cannot be properly reproduced by basic one-dimensional models (e.g., Arnett & Meakin 2011). However, as also discussed in Paper I, all those uncertainties do not modify the general conclusions of this work on the impact of the ^{12}C+^{12}C rate uncertainty, for both the stellar structure and the nucleosynthesis.

4. He CORE: WEAK s-PROCESS

In massive stars, central He-burning evolves in a convective core. The nuclear reactions driving the energy generation are the 3α reaction, converting three ^{4}He nuclei into ^{12}C, and the ^{12}C(α, γ)^{16}O reaction. The most abundant species at the end of core He-burning are ^{12}C and ^{16}O (e.g., Arnett & Thielemann 1985). The ^{14}N left from the CNO cycle during the previous H-burning is fully converted to ^{22}Ne at the beginning of core He-burning, via the reaction chain ^{14}N(α, γ)^{18}F($\beta^+\nu$)^{18}O(α, γ)^{22}Ne. Therefore, the amount of ^{22}Ne produced depends on the initial abundance of the CNO species in the star (e.g., Prantzos et al. 1990a). The main source of neutrons for the s-process is ^{22}Ne, via the reaction ^{22}Ne(α, n)^{25}Mg. This occurs at the end of the He core when the He abundance drops below 10%, in the last $\sim 10^4$ yr, the central temperature becomes larger than 2.5×10^8 K, and α-capture on ^{22}Ne is efficiently activated (e.g., Raiteri et al. 1991b; The et al. 2007; Pignatari et al. 2010). As mentioned in Section 3, all models treated share the same evolution and nucleosynthesis history until central He exhaustion.

The complete calculations for the s-process were performed using the parallel version of the multizone driver of the post-processing code PPN, developed by the NuGrid research platform (http://www.astro.keele.ac.uk/nugrid) and described by Herwig et al. (2008; MPPNP). Reference sources for basic charged particle reactions, 3α and ^{12}C(α, γ)^{16}O, have been

selected in agreement with the stellar code (Fynbo et al. 2005; Kunz et al. 2002, respectively). As outlined in Section 3, the ^{22}Ne(α, n)^{25}Mg and ^{22}Ne(α, γ)^{26}Mg rates are from Jaeger et al. (2001) and Angulo et al. (1999), respectively. Neutron-capture reaction rates for stable isotopes, and also for unstable isotopes if available, are provided by the KADoNiS Web source (Dillmann et al. 2006). For neutron-capture rates not included in KADoNiS, we refer to the Basel REACLIB database, revision 20090121 (Rauscher & Thielemann 2000). The β-decay rates are provided by Oda et al. (1994) and Fuller et al. (1985) for light species, and by Aikawa et al. (2005) for species heavier than iron. Exceptions are ^{26}Al and ^{85}Kr $\beta-$decay rates, where the isomeric state and the ground state must be considered as separate species at He-burning temperatures and terrestrial rates must be used (e.g., Pignatari et al. 2010, and reference therein).

The isotopic and elemental distributions between Fe and Mo at the end of core helium burning are presented in Figure 7. For elements between iron and strontium, most of the s-process abundances in the solar system have been produced by massive stars (weak s-process component; e.g., Käppeler et al. 1982, 1994; Rauscher et al. 2002; The et al. 2007; Pignatari et al. 2010).

The overabundance of ^{16}O is reported in Figure 7, as a reference. ^{16}O is a primary isotope; therefore, its production does not change with the initial metallicity of the star. The ^{16}O observed in the solar system today is mainly produced in massive stars, in the same region of the star where the s-process yields are synthesized. Unlike primary isotopes, however, s-process yields in massive stars show a direct dependence on the initial stellar metal content, which is closer to a secondary-like nucleosynthesis (see, e.g., Tinsley 1980; Raiteri et al. 1992, for a definition of secondary nucleosynthesis and for the analysis of the metallicity dependence for the s-process in massive stars). According to Tinsley (1980), isotopes that are fully produced by the s-process in massive stars are expected to show an overabundance a factor of two higher than ^{16}O at solar metallicity. Actually, the weak s-process is not a pure secondary process (e.g., Raiteri et al. 1992; Baraffe et al. 1992; Pignatari & Gallino 2008; Nomoto et al. 2006). However, we may still use the ^{16}O overabundance as a guidance for the s-process efficiency. From Figure 7 (left panel), Cu and Ga are the elements with the highest s-process production. In the right panel, the isotopes show an odd–even pattern typical of the s-process, due to their neutron-capture cross sections behavior (see, e.g., Käppeler et al. 1982). Among the others, the isotopes ^{58}Fe and ^{63,65}Cu show the highest overabundances, just above the iron seeds. As expected, the s-process efficiency drops beyond the Sr–Y–Zr neutron magic peak ($N = 50$), due to the total amount of neutrons produced. In Table 4, we report the abundances of the main He core products ^{12}C and ^{16}O, of the main neutron source ^{22}Ne, of the s-process seed ^{56}Fe, of the s-only isotopes between Fe and Sr, and of neutron magic ^{88}Sr at the He exhaustion. Note that the amount of ^{22}Ne available before the s-process starts is about 1% by mass (given mostly by the initial CNO) and that 36% of it is still available for more s-processing during the following C-burning phase.

The abundance of ^{54}Fe is also reported in Table 4, together with the neutron exposure. The neutron exposure τ_n is calculated according to the formula proposed by Woosley & Weaver (1995) and it is given by the ^{54}Fe depletion via neutron capture (note that ^{54}Fe is destroyed by neutron capture):

$$\tau_n = -(\text{MACS}_{^{54}\text{Fe}(n,\gamma)})^{-1} \times \ln(X(54)/X(54)_{\text{ini}}) \,(\text{mbarn}^{-1}),$$
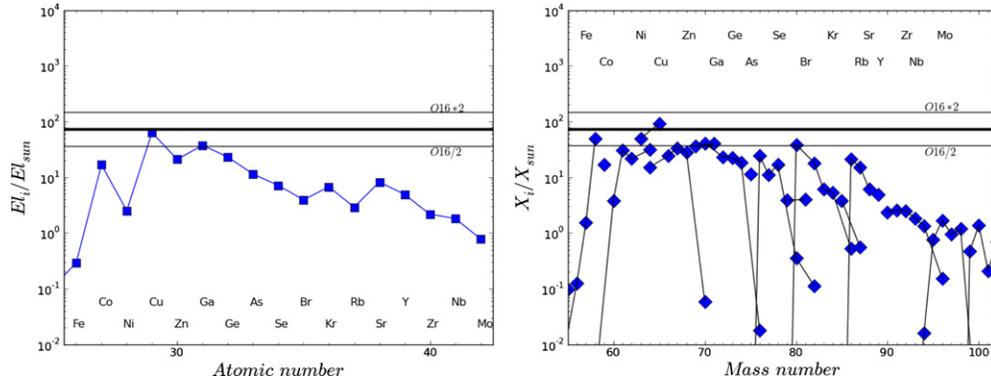
Figure 7. Left panel: overabundances for elements between Fe and Mo at the end of the core He exhaustion for the 25 $M_\odot$ star, half solar metallicity. Right panel: for the same model and for the same elements the distribution of stable isotopes is given, including the decay of unstable species. In both panels, the overabundance of ^{16}O is provided as reference, together with its value multiplied and divided by a factor of two (indicated with the labels $O16*2$ and $O16/2$ in the plots).

(A color version of this figure is available in the online journal.)

Table 4
Initial Abundances and Abundances at He Exhaustion for the Present
Stellar Model (25 $M_\odot$ Star and $Z = 0.01$) Are Given for
a Sample of Indicative Species

X_i	Initial	Central He Exhaustion
C 12	1.748E−3	0.267
O 16	4.379E−3	0.714
Ne 22	1.001E−2	3.617E−3
Fe 54	5.339E−5	5.463E−7
Fe 56	8.692E−4	2.731E−4
Ge 70	3.392E−8	1.373E−6
Se 76	9.134E−9	1.896E−7
Kr 80	2.132E−9	6.089E−8
Kr 82	1.092E−8	1.509E−7
Sr 86	4.215E−9	9.239E−8
Sr 87	3.204E−9	5.231E−8
Sr 88	3.613E−8	2.892E−7
		τ_n (mbarn^{-1})
		0.149

Notes. For the initial abundance of ^{22}Ne, the CNO species contribution to its abundance is taken into account. Finally, the neutron exposure τ_n is given at the bottom of the table.

where the MACS$_{^{54}\mathrm{Fe}(n,\gamma)}$ is the Maxwellian-averaged neutron-capture cross section on ^{54}Fe (for simplicity hereinafter in this formula, we choose for every temperature the rate at 30 keV by Coquard et al. 2006, 30.03 mbarn^{-1}), $X(54)$ is the present ^{54}Fe mass fraction and $X(54)_{\mathrm{ini}}$ is its initial abundance ($X(54)_{\mathrm{ini}} = 5.339 \times 10^{-5}$). The total neutron exposure at the end of the He core is reported in Table 4. Final mass fraction abundances of ^{12}C and ^{16}O are 0.27 and 0.71, respectively.

5. CARBON BURNING NUCLEOSYNTHESIS AND s-PROCESS

As discussed in Section 3, increasing the ^{12}C + ^{12}C rate results in an early central C ignition. This is because increasing the rate affects the equilibrium between the energy generation due to C fusion reaction and the energy lost by neutrinos. Therefore, the total lifetime of the central C-burning is affected and more massive stars may develop a convective C core (see Paper I). On the other hand, a lower ^{12}C + ^{12}C rate delays the C-burning activation to higher temperature and density conditions (see, e.g., Gasques et al. 2007). In the following section, we analyze the impact of these features on s-process nucleosynthesis.

5.1. The s-process Nucleosynthesis in C-burning Conditions, and the cs-component

In Figure 8, we present the abundances for a sample of species at the end of central O-burning as a function of the mass coordinate, for the models CU, CF88t10, CF88, CF88d10, and CL. Together with light isotopes indicative of different burning regions (^{1}H, ^{4}He, ^{12}C, ^{16}O, and ^{20}Ne), we report the abundance profile of the s-only isotopes ^{70}Ge, ^{80,82}Kr, r-only isotope ^{70}Zn (which can also be produced by direct neutron capture via the ^{69}Zn branching and is therefore a good tracer for neutron densities higher than $\sim 10^{11}$ cm^{-3}), and the isotopes ^{88}Sr, ^{138}Ba, and ^{208}Pb. These last three nuclides belong to the three neutron magic peaks along the neutron-capture path ($N = 50, 82,$ and 126, respectively), and are mostly of s-process origin. However, the bulk of their s-process abundance in the solar system distribution was produced by low-mass asymptotic giant branch (AGB) stars, which are responsible for the main and strong s-process components (see Gallino et al. 1998, and reference therein). By comparing the abundances of these isotopes in the stellar envelope (which roughly coincides with the initial abundance) with the abundances in the O-rich zone, the s-process efficiency producing these species can be deduced. In all cases, the production of ^{88}Sr is significantly higher than ^{138}Ba and ^{208}Pb, as expected from the neutron exposure regime typical for the s-process in massive stars (e.g., Raiteri et al. 1991a). The further s-process contribution during C-burning over the He core ashes may be observed in Figure 8 by comparing the abundances in the He core window with the deeper profiles in the convective C shell region. Production of ^{70}Zn, as well as the isotopic ratio ^{80}Kr/^{82}Kr, provides an indication of the neutron densities reached during the convective He-burning core, in the He core window, and in the C shell material. This is due to the effect of neutron-capture branching points at ^{69}Zn and ^{79}Se (e.g., Pignatari et al. 2010, and reference therein). In particular, ^{70}Zn and ^{80}Se both increase with increasing the neutron density. In Table 5, we report the mass-fraction abundances for a sample of species in the C shell (including the ones listed above) and for the cases reported in Figure 8.

The abundances of the main products of C-burning, ^{20}Ne and ^{23}Na, do not show a linear correlation with the C-burning rate. In particular, the ^{20}Ne/^{23}Na isotopic ratio ranges from about 12 (model M25CU) to 50 (model M25CF88d10). The maximum abundance of ^{20}Ne is obtained in M25CF88t10, whereas the largest ^{23}Na amount is in M25CU, since in this last case the
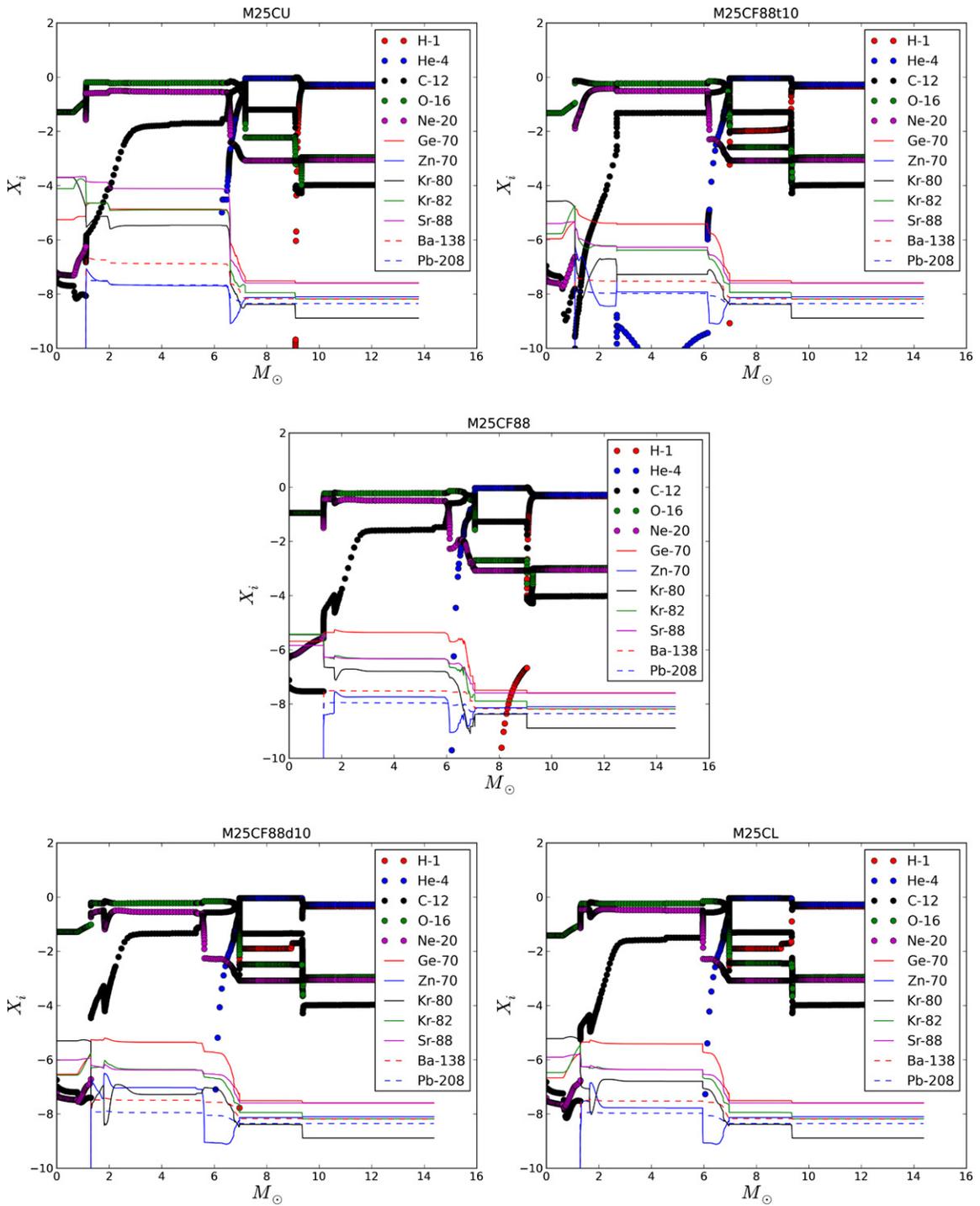
Figure 8. Abundance distribution (in mass fraction) for a sample of selected species close to the end of central O-burning is given as a function of the mass coordinate (solar masses unit) for the models considered. The model is identified by the label on top of each panel.

(A color version of this figure is available in the online journal.)

abundances are dominated by the C-burning at lower central temperatures (Arnett 1972). The distribution of light species in the C-burning region is important for the *s*-process, since 90% or more of the neutrons produced are captured by light neutron poisons (e.g., Pignatari et al. 2010). Therefore, the abundances of light nuclides need to be considered to preserve the consistency of nucleosynthesis calculations. In particular, at metallicities close to solar, the main neutron poison is ^{25}Mg, with an important contribution from ^{24,26}Mg, ^{20,22}Ne, and ^{23}Na.

From Table 5, we see that for model CF88d10 the C shell material is exposed to the highest neutron density. This is because of the late C-burning activation at higher temperature and density (see later in this section and Gasques et al. 2007). On the other hand, the *s*-process is more efficient in the CU model; compared with the standard case, the ^{88}Sr abundance is boosted by more than two orders of magnitude. Such a result has already been mentioned (Bennett et al. 2010) and is discussed in more detail in Paper I.

Table 5
Pre-explosive Abundances in the Convective C Shell Region of the Models
M25CF88d10, M25CL, M25CF88, M25CF88t10, and M25CU (Columns 2–6,
Respectively) for a Sample of Selected Species

X_i	M25CF88d10	M25CL	M25CF88	M25CF88t10	M25CU
C 12	4.546E−02	2.626E−02	2.589E−02	5.783E−03	1.651E−02
O 16	6.011E−01	5.814E−01	5.998E−01	5.724E−01	6.168E−01
Ne 20	2.861E−01	3.332E−01	3.234E−01	3.571E−01	2.951E−01
Ne 22	9.342E−05	1.498E−04	1.132E−04	9.748E−05	2.022E−03
Na 23	5.716E−03	8.421E−03	8.234E−03	7.744E−03	2.517E−02
Fe 54	7.761E−08	8.764E−08	7.571E−08	8.567E−08	6.951E−08
Fe 56	1.100E−04	1.175E−04	1.113E−04	1.140E−04	6.898E−05
Zn 70	9.146E−08	1.693E−08	1.836E−08	4.729E−08	2.071E−08
Ge 70	4.332E−06	3.881E−06	4.366E−06	4.062E−06	1.345E−05
Se 76	7.816E−07	6.063E−07	6.862E−07	6.223E−07	6.505E−06
Kr 80	5.154E−08	1.616E−07	1.605E−07	2.580E−08	3.372E−06
Kr 82	4.377E−07	4.336E−07	4.767E−07	3.387E−07	1.266E−05
Sr 88	4.196E−07	4.370E−07	4.660E−07	5.576E−07	7.740E−05
Y 89	9.578E−08	8.965E−08	9.595E−08	1.046E−07	1.709E−05
Zr 96	7.669E−09	2.214E−09	2.732E−09	2.178E−09	4.552E−08
Te124	9.139E−10	1.005E−09	1.009E−09	7.768E−10	6.765E−08
Xe130	1.087E−09	1.223E−09	1.211E−09	1.131E−09	4.824E−08
Xe134	9.884E−10	1.893E−10	2.164E−10	5.124E−10	7.992E−10
Ba138	3.196E−08	2.981E−08	3.026E−08	3.021E−08	1.322E−07
Al 26	1.690E−09	8.470E−09	6.728E−10	2.274E−06	1.367E−08
Fe 60	4.605E−06	1.132E−06	2.450E−06	3.326E−06	9.021E−08

Interestingly, all models show an overproduction of ^{88}Sr in the central zone, at a mass coordinate lower than 2 $M_\odot$, compared with more external C-burning regions. Indeed, during both Ne-burning and early O-burning conditions, ^{88}Sr is still produced, or at least not efficiently depleted, in conditions of partial photodisintegration. Also, typical p-rich species, e.g., ^{78}Kr or ^{84}Sr, are produced in this phase with different efficiencies. Such nuclear species will be further created or destroyed by photodisintegrations in later O-burning and Si-burning evolutionary stages (e.g., Thielemann & Arnett 1985). However, as pointed out by Rauscher et al. (2002), such pre-explosive abundances could be mixed by the merging of different shells into more external regions of the star, where they can survive and provide a significant contribution to p-process species yields, together with the explosive p-process abundances. Such contributions can also be relevant for non-p-rich isotopes like ^{88}Sr. Along similar lines, Arnett & Meakin (2011) showed how multi-dimensional effects may affect the stellar structure before the supernova (SN) explosion, allowing a more efficient exchange of material between different burning zones deep in the star compared with standard one-dimensional models. Therefore, caution must be maintained concerning nucleosynthesis abundances in the later evolutionary stages of massive stars.

The CF88d10 model is characterized by a lower production of neutrons compared with the CF88 model (^{88}Sr is lower by 11%), but it has a higher neutron density (higher ^{70}Zn amount, lower ^{80}Kr/^{82}Kr ratio; see Table 5). This effect was discussed by Gasques et al. (2007). The CL and CF88 models show similar results, because of the similarities between the two stellar models (Section 3). The CF88t10 model shows an increase of ^{88}Sr by only a factor of 1.2 in the final convective C shell compared to CF88 (Table 5), confirming earlier results presented by Bennett et al. (2010). In the CU case, ^{88}Sr increases by a factor of 166 relative to the standard case. Major differences are observed for the whole s-process distribution.

The reason for such a large overproduction in the CU case is the strong s-process efficiency reached in the convective C-burning core. For CU, in the C core the dominant neutron source is ^{13}C(α, n)^{16}O, not ^{22}Ne(α, n)^{25}Mg. When the burning temperature is lower than ∼0.70–0.75 GK, ^{13}C is efficiently produced via the ^{12}C(p, γ)^{13}N($\beta^+\nu$)^{13}C channel. The ashes of the C core are later mixed in the convective C shell and ejected in the interstellar medium by the final SN explosion (Figure 2). For the CU ^{12}C+^{12}C rate, the overlap between the convective core and the final shell acts to drastically increase the s-process efficiency, as explained in Paper I.

The activation of the ^{13}C(α, n)^{16}O reaction in the C-burning core was previously discussed by Chieffi et al. (1998). However, in stellar models using the standard ^{12}C+^{12}C rate, the central C-burning is not convective. Even in the eventuality that a small convective core is developed, the enriched material is further processed by the more advanced burning phases and eventually collapses to form the neutron star. On the other hand, when the temperature is higher than ∼0.70–0.75 GK, ^{13}N(γ, p)^{12}C reaches equilibrium with its direct reaction (Clayton 1968). In these conditions, the only way to produce ^{13}C is via ^{12}C(n, γ)^{13}C, and so the ^{13}C(α, n)^{16}O reaction only recycles neutrons captured by ^{12}C. The neutrons have to be produced by other reactions, e.g., by ^{22}Ne(α, n)^{25}Mg.

In Figure 9 (left panel), the final s-process elemental distribution between Fe and La is shown for all models considered. The first four cases present similar s-process abundance distributions. In Table 6, the overproduction factors for elements between C and Mo are reported for a detailed comparison. The CU model produces an s-process distribution that is peaked in the region of Sr–Y–Zr–Nb (with an overproduction factor larger than 1000 for Sr and Y). The neutron magic peak at $N = 50$ is bypassed by the neutron-capture path efficiently and a relevant production of s elements (with an overproduction factor larger than 100) is observed up to Sn ($Z = 50$). Negligible abundances are observed above Ba–La ($Z = 56, 57$), compared with the Sr–Y–Zr–Nb bulk. In Figure 9 (right panel), the respective isotopic distributions between Fe and Mo are presented. We recall again that the different distributions shown in Figure 9 share the same neutron-capture process history until the end of the core He-burning. After core He exhaustion, the heavy isotope distribution in the C shell ejecta is driven by different neutron exposure histories.

In the CF88 model, any ^{22}Ne left in the He core ashes is burnt with a peak neutron density of ∼10^{11} cm^{-3} (e.g., Raiteri et al. 1991a) and a neutron exposure of $\tau \sim 0.05$ mbarn^{-1}. The final convective C-burning shell episode is switched off by the onset of central O-burning and is not active in the last evolutionary phase before the SN explosion. The final distribution in Figure 9 is peaked in the Cu–Ga–Ge region. In the CU model, the dominant neutron exposure contribution is provided during the convective C-burning core, driven by the ^{13}C(α, n)^{16}O reaction. During the final convective C shell, ^{22}Ne drives the neutron flux. The component built in the C core and peaked in the Sr–Y–Zr–Nb region is dominant in the final s-process rich ejecta because of the larger neutron exposure and the large overlapping factor between the core and shell (∼2/3 of the mass of the convective C shell is made of C-burning core ashes). Similar results were found in Paper I for a large range of masses using the CU rate, and for the specific case of the 20 $M_\odot$ star model and a rate intermediate between CF88 and CU (CI rate; Paper I). In cases where the convective C core overlaps with the final convective C shell, the material
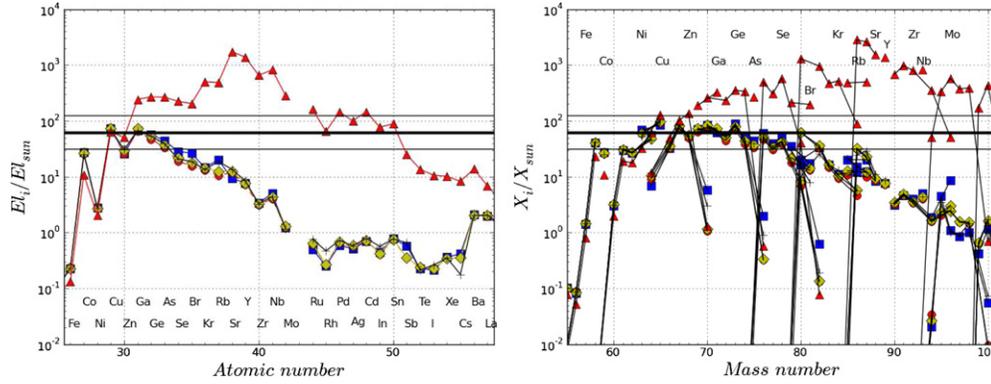
Figure 9. Left panel: the final element production factors between Fe ($Z = 26$) and La ($Z = 57$) in the C shell region for CF88d10 (blue squares), CL (red circles), CF88 (yellow diamonds), CF88t10 (black crosses), and CU (red triangles). Right panel: the isotopic distribution zoomed in the mass region between ^{56}Fe and ^{100}Mo, for the same stellar models as presented in the left panel. Isotopes of a given element are connected with lines.
(A color version of this figure is available in the online journal.)

Table 6
Pre-explosive Element Overabundances in the Convective C Shell Region
from C to Mo for the Models M25CF88d10, M25CL, M25CF88,
M25CF88t10, and M25CU (Columns 2–6, Respectively)

$X_{el}/X_\odot$	M25CF88d10	M25CL	M25CF88	M25CF88t10	M25CU
C	1.311E+01	7.575E+00	7.470E+00	1.668E+00	4.763E+00
N	5.139E−04	8.662E−03	9.398E−03	5.553E−03	3.202E−02
O	6.230E+01	6.025E+01	6.215E+01	5.932E+01	6.392E+01
F	1.369E−02	2.631E−02	2.518E−02	3.063E−02	2.652E−01
Ne	1.454E+02	1.694E+02	1.644E+02	1.816E+02	1.520E+02
Na	1.429E+02	2.105E+02	2.059E+02	1.936E+02	6.293E+02
Mg	7.433E+01	6.250E+01	5.587E+01	7.081E+01	5.192E+01
Al	2.613E+01	2.974E+01	2.849E+01	2.782E+01	5.220E+01
Si	6.938E+00	3.961E+00	3.366E+00	4.117E+00	1.979E+00
P	1.146E+01	8.229E+00	8.065E+00	7.423E+00	1.240E+01
S	3.506E−01	3.216E−01	3.161E−01	3.153E−01	2.560E−01
Cl	2.498E+00	2.814E+00	2.818E+00	2.901E+00	3.259E+00
Ar	3.586E−01	3.568E−01	3.575E−01	3.552E−01	3.280E−01
K	2.368E+00	2.137E+00	2.172E+00	2.068E+00	2.111E+00
Ca	2.273E−01	2.315E−01	2.282E−01	2.292E−01	1.836E−01
Sc	1.154E+01	9.397E+00	9.780E+00	9.859E+00	1.180E+01
Ti	9.323E−01	9.359E−01	9.576E−01	9.415E−01	1.798E+00
V	5.069E−01	4.622E−01	4.823E−01	4.784E−01	1.069E+00
Cr	3.439E−01	3.521E−01	3.474E−01	3.494E−01	2.950E−01
Mn	1.032E−01	1.028E−01	1.013E−01	1.030E−01	7.756E−02
Fe	2.260E−01	2.372E−01	2.292E−01	2.328E−01	1.335E−01
Co	2.741E+01	2.589E+01	2.634E+01	2.521E+01	1.079E+01
Ni	2.759E+00	2.740E+00	2.752E+00	2.715E+00	2.069E+00
Cu	7.410E+01	7.078E+01	7.259E+01	6.934E+01	6.346E+01
Zn	2.602E+01	2.623E+01	2.946E+01	3.074E+01	5.052E+01
Ga	6.785E+01	6.604E+01	7.312E+01	6.709E+01	2.436E+02
Ge	5.763E+01	4.726E+01	5.341E+01	5.323E+01	2.692E+02
As	4.441E+01	3.353E+01	3.787E+01	3.913E+01	2.659E+02
Se	2.852E+01	1.896E+01	2.179E+01	2.088E+01	2.248E+02
Br	2.629E+01	1.554E+01	1.814E+01	1.876E+01	2.049E+02
Kr	1.455E+01	1.308E+01	1.441E+01	1.344E+01	5.039E+02
Rb	2.022E+01	1.065E+01	1.257E+01	1.875E+01	4.854E+02
Sr	9.261E+00	1.182E+01	1.249E+01	1.365E+01	1.739E+03
Y	7.791E+00	7.293E+00	7.805E+00	8.507E+00	1.390E+03
Zr	3.394E+00	3.103E+00	3.327E+00	3.258E+00	6.575E+02
Nb	5.012E+00	4.053E+00	4.407E+00	4.401E+00	8.198E+02
Mo	1.224E+00	1.245E+00	1.316E+00	1.179E+00	2.866E+02

from the core dominates the final s-process ejecta. The resulting s-process yields are anomalous compared with the classical weak s-process component.

If all, or most, of the s-process-rich material lost to the interstellar medium by core collapse SNe is similar to the CU

ejecta, then the predicted abundances cannot be reconciled with the solar system distribution. In other words, if all massive stars were to eject material exposed to ^{13}C(α, n)^{16}O in the central C-burning conditions observed for CU, an anomalous abundance distribution would be observed. This may indicate that the upper limit ^{12}C+^{12}C rate is overestimated, a conclusion already reached in Paper I. We will discuss in Section 6 the impact of the ^{12}C(^{12}C, α)^{20}Ne and ^{12}C(^{12}C, p)^{23}Na strength uncertainty on these results. Tackling the discussion from a more speculative point of view, two s-process components may be identified: the standard weak s-process component, dominated by ^{22}Ne(α, n)^{25}Mg, and a stronger s-process component coming from ^{13}C(α, n)^{16}O, triggered when the temperature is low enough to prevent the ^{13}N(γ, p)^{12}C reaction from becoming efficient. We refer to the latter component as the "cold" C-burning component or "cs-component" hereafter.

5.2. Possible Implications of the cs-component for the Lighter Element Primary Process

Travaglio et al. (2004) performed Galactic chemical evolution (GCE) calculations, which included s-process contributions from massive and low-mass AGB stars and the r-process signature evaluated from the r-process residual and from spectroscopic observations at low metallicity. A new unknown component was identified in the solar system distribution (termed the lighter element primary process or LEPP), spanning the region from Sr–Y–Zr to ~Te–Xe. The LEPP component comprises 10%–20% of the total elemental abundances in the region, including a similar contribution to the s-only species. This component has been connected to the anomalous abundances observed in a group of very low metallicity stars that are enriched in the Sr–Y–Zr mass region compared with the r-process (see also recent observations by Hansen & Primas 2011; Chiappini et al. 2011). Besides the s-process, various scenarios involving primary explosive nucleosynthesis in massive stars have been invoked (e.g., Hoffman et al. 1996; Fröhlich et al. 2006; Qian & Wasserburg 2007; Montes et al. 2007; Pignatari & Gallino 2008; Farouqi et al. 2009, 2010; Roberts et al. 2010; Arcones & Montes 2011).

Is it possible that the cs-component corresponds to or partially explains the LEPP component? In other words, if only a limited fraction of s-process-rich material with the distinct ^{13}C(α, n)^{16}O signature is ejected from massive stars, could this be a feasible scenario to explain LEPP in the solar system? According to Paper I, it is possible that the cs-component is only ejected for a

limited range of stellar masses. By using a ^{12}C+^{12}C rate given by the geometric average between CU and CF88 (CI), it was found that only a 20 $M_\odot$ star ejects material carrying the *cs*-component signature, and all other models displayed the standard weak *s*-process signature. From Table 6, oxygen overproduction is ∼60. Therefore, at solar metallicity an element is fully produced by a secondary *s*-process if its overabundance is ∼120, and 20% of its production is explained if the overproduction is ∼24 (see discussion in Section 4). The *cs*-component in CU is peaked at Sr–Y–Zr, where the overproduction of Sr is ∼1740 (Table 6). This means that if only $f = 1\%$–2% of the *s*-process-rich material ejected by massive stars carries a cs-like component, ∼20% of the solar Sr could be explained. The factor f could correspond to the contribution from a narrow mass range of stars, for instance. Note that the current astrophysics scenario for elements typically produced by the weak *s*-process would not be compromised, since with $f = 0.02$ the *cs*-component contribution to Cu or Ga would be marginal (∼1% and ∼5% of their solar abundances, respectively). Only Sr, Y, Zr, and Nb would receive a significant contribution by the *cs*-process in this case (see Table 6 for comparison).

Such considerations provide a warning to bear in mind in our discussion and more generally for the present understanding of the *s*-process in massive stars. If the ^{12}C+^{12}C rate is higher than presently used, and the *cs*-process does exist, only 1%–2% of the *s*-process-rich material ejected from massive stars carrying such a component would be enough to explain the LEPP signature at the Sr peak. Therefore, it is extremely important to measure the ^{12}C+^{12}C rate down to stellar energies, to constrain C-burning conditions and *s*-process yields from massive stars.

5.3. Pre-explosive Production of ^{26}Al and ^{60}Fe

In Table 5, we report our ^{26}Al and ^{60}Fe predictions for the different models. In particular, using a weaker ^{12}C+^{12}C rate, Gasques et al. (2007) noted a stronger production in the total stellar yields of these long-lived radio nuclides compared with standard models. This is characteristic of the higher proton and neutron density, which affects the convective C shell abundances. We confirm this trend for ^{60}Fe pre-explosive production. Indeed, because of the long half-life at stellar C-burning temperatures (few tens of years; e.g. Langanke & Martínez-Pinedo 2000), ^{60}Fe can be produced and maintained in stellar material even if the convective C-burning shell ends before the SN explosion, which is the case for all of our models except CF88t10. In Table 5, CF88d10 shows the highest ^{60}Fe abundance compared with the other models. On the other hand, CU has the lowest abundance (about a factor of 50 less than in CF88d10). During C-burning, the ^{58}Fe abundance (the main seed of ^{60}Fe) is mostly depleted compared to other models. The ^{60}Fe is not efficiently produced in the C core because of the lower neutron density compared with the convective C shell, resulting in a weaker neutron capture channel at the ^{59}Fe branching. Consequently, the pre-explosive contribution to the final ^{60}Fe ejecta tends to be inversely proportional to the ^{12}C+^{12}C rate, increasing as the rate decreases.

The pre-explosive ^{26}Al abundance in the C shell region is not significantly enhanced in the CF88d10 model. In fact, the ^{26}Al half-life at C-burning temperatures is quite low (few tens of minutes; e.g. Oda et al. 1994), allowing it to almost completely decay in stellar material before the SN explosion. The model showing the highest pre-explosive ^{26}Al abundance is CF88t10, the only one in the present set of models having a convective C shell lasting until the latest evolutionary phases before the onset
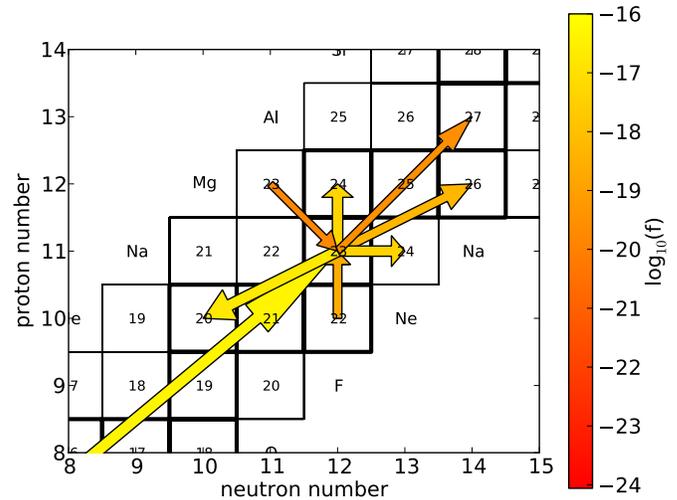
Figure 10. Nucleosynthesis fluxes ($[\delta Y_i/\delta t]_j$, i.e., the variation of the abundance $Y_i = X_i/A_i$ due to the reaction j) producing and depleting ^{23}Na are shown in central C-burning conditions. The arrow size and color correspond to the flux strength.

(A color version of this figure is available in the online journal.)

of core collapse. This stellar structure feature is in common with the stellar models used by Gasques et al. (2007).

To first order, the pre-explosive ^{60}Fe abundance correlates with the neutron density in the final convective C shell, and is anti-correlated with the *s*-process efficiency of the CU model, where most of the neutrons are produced during earlier central C-burning. Conversely, the dependence of the pre-explosive ^{26}Al abundance on the ^{12}C+^{12}C rate is model dependent. For a more comprehensive discussion about the production of ^{26}Al and ^{60}Fe in massive stars, we refer to, e.g., Timmes et al. (1995a) and Limongi & Chieffi (2006), where the explosive component is also taken into account.

6. ^{12}C(^{12}C, α)^{20}Ne AND ^{12}C(^{12}C, p)^{23}Na CHANNELS

The ^{12}C+^{12}C reaction has two main channels with comparable strength, producing respectively one α particle and one ^{20}Ne nucleus, or one proton and one ^{23}Na nucleus. However, the predicted C-burning yields consist of more than 20% ^{20}Ne, and only few per cent of ^{23}Na. This is due to the efficient activation of ^{23}Na(p, α)^{20}Ne, which processes ^{23}Na in ^{20}Ne (e.g., Arnett & Thielemann 1985; Chieffi et al. 1998). As an example, in Figure 10, we show the isotopic chart with the main reaction fluxes responsible for productive and destructive nucleosynthesis of ^{23}Na, at typical shell C-burning conditions. Most of the ^{23}Na produced via ^{12}C(^{12}C, p)^{23}Na is depleted by the ^{23}Na(p, α)^{20}Ne reaction. Therefore, the final ^{23}Na abundance is mostly given by the equilibrium between those two reactions. The other significant flux in Figure 10 is due to the ^{23}Na(p, γ)^{24}Mg reaction, which competes with the (p, α) channel (with a typical flux ratio of (p, α)/(p, γ) ∼ 4; e.g., NACRE). Note that most of the sodium observed today in the solar system is produced in massive stars in the conditions described.

At stellar temperatures, the uncertainty in the relative strength between the ^{24}Mg* α-decay and proton-decay channels has a relevant impact on nucleosynthesis calculations. In the present work, we use the ratio $R_\alpha/R_p = 0.65/0.35$, keeping in mind that we also properly consider the small contribution from the neutron channel (see Section 7 for a more detailed discussion
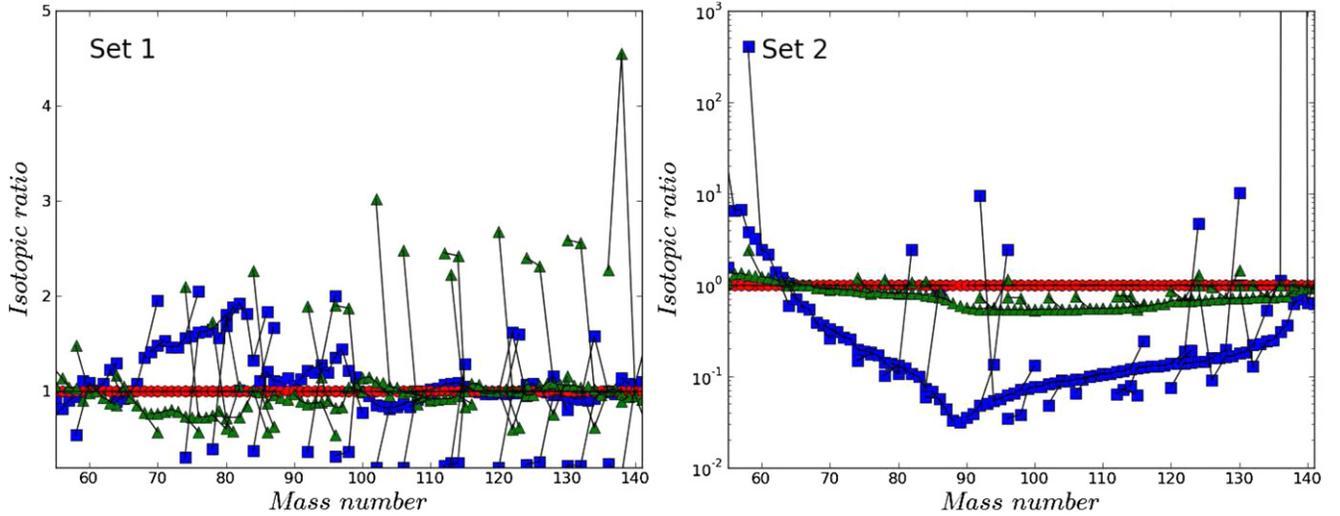
Figure 11. Left panel: the isotopic abundances at the end of C-burning (when the mass fraction of ^{12}C left is less than 2%) for the cases using the ^{12}C+^{12}C channel ratio $R_\alpha/R_p = 0.05/0.95$ (green triangles) and $R_\alpha/R_p = 0.95/0.05$ (full blue squares), normalized to the isotopic distribution obtained using the standard $R_\alpha/R_p = 0.65/0.35$. Species belonging to the same element are connected with lines. The temperature and density used for the calculations are $T = 1.0$ GK and $\rho = 10^5$ cm^{-3}; the ^{12}C+^{12}C rate used is CF88 (*set* 1). Right panel: as in the left panel, but for $T = 0.65$ GK and $\rho = 10^4$ cm^{-3} and the ^{12}C+^{12}C CU rate (*set* 2). Note that the relative abundance distributions are shown with a different scale in the *y*-axis compared with the left panel.

(A color version of this figure is available in the online journal.)

about the neutron channel). However, this ratio becomes more uncertain at temperature conditions closer to the Gamow peak energies and typical C core conditions.

In order to test the impact of this uncertainty, we have performed two sets of calculations using a simple single-zone post-processing method: using the CF88 ^{12}C+^{12}C rate (*set* 1, CF88 rate; $T = 1.0$ GK, $\rho = 10^5$ g cm^{-3}) for typical shell C-burning conditions and the CU rate for conditions dominated by core C-burning (*set* 2, CU rate; $T = 0.65$ GK, $\rho = 10^4$ g cm^{-3}), the ratio R_α/R_p has been modified within the range $0.95/0.05 \lesssim R_\alpha/R_p \lesssim 0.05/0.95$. In Figure 11, the C-burning yields from the most extreme cases are compared with the yields obtained using the standard ratio 0.65/0.35. Results for *set* 1 and *set* 2 are presented in the left and right panels, respectively. For a more direct comparison, in Table 7 the abundances for selected species corresponding to the cases presented in Figure 11 are reported.

Concerning *set* 1, despite the large difference in the R_α/R_p ratio, the variation is below a factor of two for most species. A larger departure from the standard isotopic distribution is related to *p*-process species (e.g., ^{92}Mo), which are only depleted by neutron captures and have in all cases negligible abundances. Increasing the number of α particles compared with protons has the effect of increasing the number of neutrons available, therefore increasing the *s*-process efficiency. In particular, the *s*-process species between Fe and Zr are boosted (see Table 7). On the other hand, increasing the number of protons reduces the *s*-process efficiency, even if protons are mostly converted to α particles via ^{23}Na$(p,\alpha)^{20}$Ne. The main reason for this behavior is that in C-burning conditions the ^{22}Ne$(\alpha, n)^{25}$Mg nucleosynthesis channel competes with ^{22}Ne$(p, \gamma)^{23}$Na. This is shown in Figure 12 for the standard case *set* 1, where the fluxes producing and depleting ^{22}Ne are presented. Therefore, variation of the R_α/R_p ratio also affects ^{22}Ne nucleosynthesis. Note that during C-burning the ^{22}Ne$(\alpha, \gamma)^{26}$Mg rate is marginal compared with the (α, n) rate.

In Figure 11 (right panel), *set* 2 calculations show a larger variation than *set* 1. In particular, a stronger ^{12}C+^{12}C proton
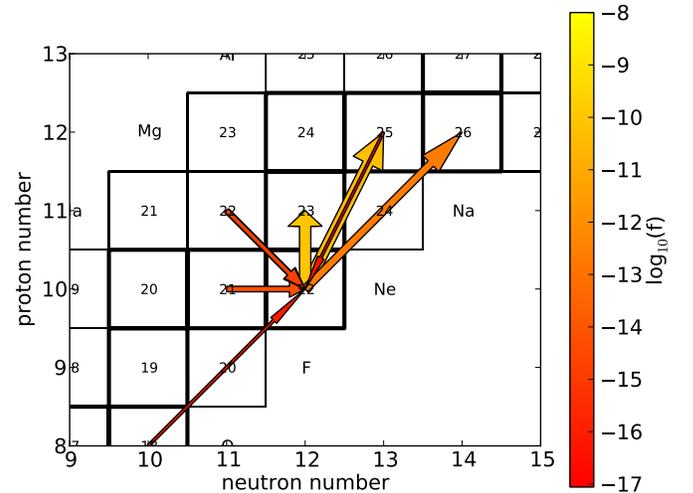
Figure 12. Nucleosynthesis fluxes producing and depleting ^{22}Ne are shown in shell C-burning conditions. The arrow size and color correspond to the flux strength.

(A color version of this figure is available in the online journal.)

channel does not significantly modify the *s*-process yields and the results discussed in Section 5 are confirmed. Conversely, a stronger α channel reduces the *s*-process yields by more than a factor of 10 at the Sr–Y–Zr peak. For instance, ^{88}Sr (neutron magic number, $N = 50$) in the a95p05* case (where α-channel probability = 95%, proton-channel probability = 5%) is reduced by a factor of ~30 compared with the st* case (α-channel probability = 65%, proton-channel probability = 45%; see Table 7). This effect is the opposite to that in *set* 1, where a stronger α channel leads to a more efficient *s*-process production. The main neutron source in *set* 2 (and the *s*-process ejecta when using the CU ^{12}C+^{12}C rate) is the ^{13}C$(\alpha, n)^{16}$O, not ^{22}Ne$(\alpha, n)^{25}$Mg. In the temperature conditions of *set* 2, the photodisintegration timescale of ^{13}N via ^{13}N$(\gamma, p)^{12}$C is comparable with the β-decay of ^{13}N to ^{13}C (see Section 5).

Table 7
Selected Abundances at the Central He Exhaustion and for C-burning Nucleosynthesis Tests,
Using Different ^{12}C(^{12}C, α)^{20}Ne and ^{12}C(^{12}C, p)^{23}Na Relative Strengths

X_i	He Ashes	a05p95	st	a95p05	a05p95*	st*	a95p05*
C-12	2.673E−01	1.544E−02	1.544E−02	1.543E−02	1.999E−02	1.998E−02	2.000E−02
O-16	7.142E−01	5.791E−01	5.708E−01	5.658E−01	7.131E−01	6.478E−01	5.883E−01
Ne-20	5.026E−03	3.412E−01	3.639E−01	3.792E−01	1.241E−01	2.475E−01	3.419E−01
Ne-22	3.617E−03	1.166E−04	1.214E−04	1.123E−04	4.610E−03	3.887E−03	1.824E−03
Na-23	1.594E−04	1.970E−02	1.188E−02	4.171E−03	8.534E−02	3.898E−02	9.133E−03
Fe-54	5.463E−07	3.170E−07	2.430E−07	1.592E−07	1.079E−09	5.799E−10	3.359E−08
Fe-56	2.731E−04	2.117E−04	1.867E−04	1.526E−04	1.397E−05	1.060E−05	6.937E−05
Zn-70	1.040E−09	4.392E−09	7.682E−09	1.502E−08	2.886E−08	3.266E−08	8.577E−09
Ge-70	1.373E−06	2.206E−06	2.877E−06	4.258E−06	2.731E−05	2.989E−05	9.892E−06
Se-76	1.896E−07	2.822E−07	3.876E−07	6.253E−07	1.064E−05	1.256E−05	2.219E−06
Kr-80	6.089E−08	9.677E−08	1.341E−07	2.265E−07	5.510E−06	6.717E−06	8.797E−07
Kr-82	1.509E−07	1.475E−07	2.034E−07	3.903E−07	1.492E−05	1.860E−05	1.980E−06
Sr-88	2.892E−07	3.375E−07	3.610E−07	3.965E−07	2.490E−05	3.939E−05	1.287E−06
Y-89	5.994E−08	7.312E−08	8.011E−08	9.123E−08	3.781E−06	6.340E−06	2.000E−07
Zr-96	2.259E−10	1.835E−09	3.414E−09	6.825E−09	5.834E−11	5.055E−11	1.240E−10
Te-124	1.609E−09	1.413E−09	1.476E−09	1.574E−09	8.149E−09	1.192E−08	1.710E−09
Xe-130	2.056E−09	1.823E−09	1.724E−09	1.612E−09	7.133E−09	9.925E−09	1.762E−09
Ba-138	3.580E−08	3.812E−08	3.910E−08	4.033E−08	6.307E−08	7.268E−08	4.711E−08

Notes. Mass fraction abundances for a sample of selected species in the He core ashes (Column 2), when the final ^{12}C is less than 2% for $set1$ cases (Column 3: where a05p95 means $R_\alpha/R_p = 0.05/0.95$; Column 4: where st means $R_\alpha/R_p = 0.65/0.35$; and Column 5: where a95p05 means $R_\alpha/R_p = 0.95/0.05$) and for $set2$ cases (Columns 6–8, labels have the same meaning as in $set1$ cases, and the symbol * is used to distinguish from $set1$). See the text for more details.

As a result, the available ^{13}C abundance depends on the amount of protons available to activate the ^{12}C(p, γ)^{13}N reaction. As such, increasing the R_α/R_p ratio with respect to the standard value reduces the proton density and consequently the ^{13}C neutron source. Calculations in $set2$ also show significant variations for light species; a stronger α-channel leads to a significant decrease of ^{16}O and ^{23}Na and an increase of ^{20}Ne (see details in Table 7). Conclusions obtained in Section 3 need to be viewed cautiously since the CU model, as well as the other four models, was calculated using a constant value of $R_\alpha/R_p = 0.65/0.45$. If the ^{12}C+^{12}C rate is indeed larger than CF88, then the impact of the R_α/R_p ratio uncertainty on stellar calculations becomes more important and may not be negligible with regard to the main features of subsequent evolutionary stages.

In summary, the total ^{12}C+^{12}C fusion rate is not the only uncertainty to consider when comparing different nucleosynthesis calculations. In this section, we showed that the R_α/R_p ratio must also be considered and that more experimental efforts are required to constrain the relative strength of the primary decay channels.

7. ^{12}C(^{12}C, n)^{23}Mg CHANNEL

Besides the two main nucleosynthesis channels, feeding ^{20}Ne and ^{23}Na, respectively, the ^{12}C+^{12}C reaction can also result in the production of neutrons via the ^{12}C(^{12}C, n)^{23}Mg channel. The isotope ^{23}Mg is unstable, decaying rapidly ($\tau_{1/2} = 11.3$ s) into ^{23}Na. The reaction is endothermic with a Q-value of -2.6 MeV and will contribute only at higher temperatures. Yet, even at high energies the contribution of the reaction branch is small. An early analysis by Dayras et al. (1977, D77 hereafter) indicates 2% at 3 MeV gradually increasing up to 10%. This is confirmed by more recent measurement (X. Tang 2012, private communication). For the present calculations, the ^{12}C(^{12}C, n)^{23}Mg rate of D77 has been used. In simulations where the total ^{12}C+^{12}C fusion rate corresponds to the CF88

rate, the neutron flux produced by the ^{12}C(^{12}C, n)^{23}Mg branch is weaker than the ^{22}Ne(α, n)^{25}Mg, at least for solar-like metallicities. Note, however, that the ^{22}Ne(α, n)^{25}Mg neutron source is secondary and its efficiency depends on the initial metal content, whereas ^{12}C(^{12}C, n)^{23}Mg is a primary source. In comparison with the third potential neutron source ^{13}C(α, n)^{16}O, the ^{12}C(^{12}C, n)^{23}Mg probability is marginal for models using the CU rate as will be discussed below.

The experimental uncertainty in the ^{12}C(^{12}C, n)^{23}Mg data is approximately 50% at energies above 4 MeV, and toward lower energies it increases up to 80%. The cross section is expected to decline rapidly since the neutron channel closes at 2.6 MeV, yet the existence of molecular resonance structures near the threshold cannot be excluded, because such features are visible in the proton and α-channels at the corresponding energy range. For low temperature environments typical for C shell burning near 1 GK, we therefore consider an uncertainty range of approximately a factor of 10; for higher temperatures as found at the bottom of the C shell during the later evolutionary stages prior to core collapse, we reduce the uncertainty range to a factor of five since the Gamow window extends into the excitation range well covered by experiment. We do not consider the reaction for typical core C-burning conditions, since the neutron channel of C-burning is endoergic and therefore suppressed toward the low temperatures associated with the core burning environment.

In order to test the impact of the neutron channel, and taking into account its uncertainty, we have performed two sets of calculations using different ^{12}C(^{12}C, n)^{23}Mg rates (D77, and D77 multiplied by a factor of 2, 5, and 10, which are called D77t2, D77t5, and D77t10, respectively): $set3$, where typical C shell conditions with constant temperature and density are considered (CF88 ^{12}C+^{12}C rate, $T_{set3} = 1.1$ GK and $\rho = 10^5$ g cm^{-3}, the ^{12}C(^{12}C, n)^{23}Mg probability is ~0.12% of the total rate), and $set4$, where realistic temperature and density profiles are extracted at the bottom of the final convective carbon
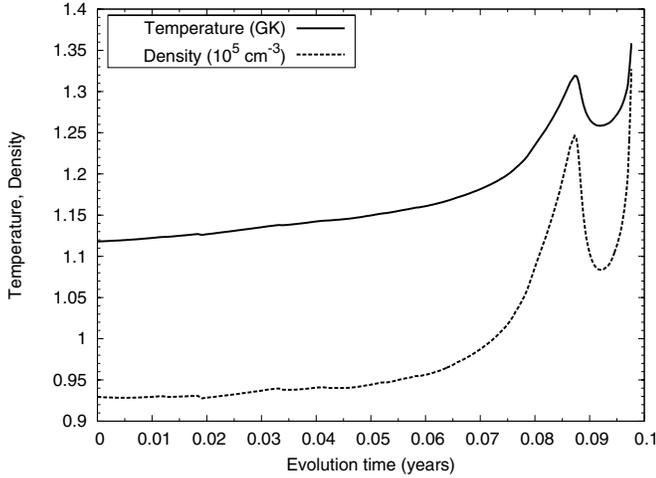
Figure 13. Temperature and density profiles at the bottom of the final convective carbon shell for the CF88t10 stellar model. Evolution time = 0 corresponds to the start of shell C-burning.

Table 8
Selected Abundances at the Central He Exhaustion and for C-buring Nucleosynthesis Tests, Using Different $^{12}C(^{12}C, n)^{23}Mg$ Probability

X_i	He Ashes	D77	D77t5	D77t10
C-12	2.673E−01	1.408E−02	1.408E−02	1.408E−02
Ne-20	5.026E−03	3.554E−01	3.532E−01	3.504E−01
Ne-22	3.617E−03	4.875E−05	6.408E−05	8.181E−05
Na-23	1.594E−04	9.919E−03	1.057E−02	1.139E−02
Fe-56	2.731E−04	1.786E−04	1.626E−04	1.451E−04
Zn-70	1.040E−09	9.198E−08	1.069E−07	1.267E−07
Ge-70	1.373E−06	3.361E−06	4.020E−06	4.827E−06
Se-76	1.896E−07	4.719E−07	5.946E−07	7.767E−07
Kr-80	6.089E−08	7.971E−08	1.174E−07	1.689E−07
Kr-82	1.509E−07	1.839E−07	2.583E−07	3.882E−07
Sr-88	2.892E−07	3.426E−07	3.487E−07	3.561E−07
Y-89	5.994E−08	8.013E−08	8.395E−08	8.826E−08
Zr-96	2.259E−10	7.393E−09	1.004E−08	1.387E−08
Te-124	1.609E−09	1.206E−09	1.377E−09	1.503E−09
Xe-130	2.056E−09	1.405E−09	1.390E−09	1.376E−09
Ba-138	3.580E−08	3.852E−08	3.872E−08	3.884E−08
msv_s	⋯	1.000E+00	1.299E+00	1.772E+00

Notes. Mass fraction abundances for a sample of selected species in the He core ashes (Column 2), and in the C shell when ^{12}C is less than 2% for *set* 3 cases: the standard case D77 (Column 3: where the $^{12}C(^{12}C, n)^{23}Mg$ rate by Dayras et al. 1977 is used), D77t5 (standard rate multiplied by 5, Column 4), and D77t10 (standard rate multiplied by 10, Column 5). The average abundance variation of the *s*-only isotopes between iron and strontium (^{70}Ge, ^{76}Se, $^{80,82}Kr$, and $^{86,87}Sr$) is provided in the last line of the table for each case considered, normalized to the D77 case (labeled msv_s in the table).

shell of the CF88t10 model (using the CF88t10 rate). Note that cases with rates lower than D77 are not considered here, since the $^{12}C(^{12}C, n)^{23}Mg$ contribution becomes negligible. The temperature and density profiles used for *set* 4 calculations are reported in Figure 13 and are characterized by an increase in the final temperature and density, up to $T = 1.36$ GK and $\rho = 1.33 \times 10^5$ g cm^{-3}. During core collapse, and shortly before the SN explosion, thermal instabilities occur in O-burning layers and temperature and density may rapidly increase in the outer stellar material (Arnett 1974; Arnett & Wefel 1978). We choose the CF88t10 model because it shows a convective C shell lasting until the SN explosion. In all of the other models considered in this work, the convective phase terminates at an earlier point in the evolution. In these cases, stellar structure modifications triggered by O ignition in the core prohibits convective shell C-burning from continuing (e.g., Hirschi et al. 2004) and the yields are not affected by the temperature increase shown in Figure 13. In the CF88t10 model, the final temperature and density rise causes a boost in the neutron density, resulting in distinctive effects in the *s*-process distribution. For instance, all the isotopes considered as *r*-only between iron and strontium may be significantly produced (^{70}Zn, ^{76}Ge, $^{80,82}Se$), ^{75}As overproduction might be comparable to neighbor *s*-only isotopes (e.g., ^{76}Se), and, in general, *s*-process branchings are significantly affected (e.g., Pignatari et al. 2010).

During this final phase, the $^{12}C(^{12}C, n)^{23}Mg$ channel may also become more efficient, since its strength compared with α and the proton channel increases with temperature (Dayras et al. 1977). The main purpose of the two sets presented in this section is to test the impact of the $^{12}C(^{12}C, n)^{23}Mg$ channel in typical C shell conditions (*set* 3) and in the final temperature-rise phase (*set* 4).

The relative isotopic distributions for the D77t2, D77t5, and D77t10 cases are shown for *set* 3 in Figure 14. The right panel shows the same calculations for *set* 4. Abundances for selected species are reported in Tables 8 and 9 for the most extreme cases, compared to D77. In both sets of calculations presented in Figure 14, the D77t2 case shows small departures from the standard case within 10%. On the other hand, in the D77t5 and D77t10 cases, the *s*-only species between iron and strontium (^{70}Ge, ^{76}Se, $^{80,82}Kr$ and $^{86,87}Sr$) show an increase in their average mass fraction of 1.30 and 1.77, respectively (Table 8). This means that the average neutron exposure has increased (see also

^{88}Sr in Table 8). Interestingly, an increase in the availability of neutrons due to a more efficient $^{12}C(^{12}C, n)^{23}Mg$ channel causes a propagation effect over the *s*-process species up to Sr, with significant differences along the neutron capture path. Illustrating this point, the variation of $^{80,82}Kr$ is larger than lighter or heavier *s*-only species (e.g., in the D77t10 case compared to the D77 case, the ^{82}Kr abundance increases by a factor of 2.1, compared with 1.4 for ^{70}Ge; Table 8). The *r*-only isotopes like ^{70}Zn or ^{76}Ge are enhanced for the cases D77t5 and D77t10 compared with the standard case, with a production comparable to the *s*-process species (see Table 8).

The evolution history of the stellar structure has a relevant impact on the C shell nucleosynthesis, affecting for example the amount of ^{12}C available when C ignites in a convective shell (e.g., Imbriani et al. 2001; El Eid et al. 2009). The *set* 4 calculations presented in Figure 14 use the initial abundances and the temperature–density evolution of the last convective C shell in the CF88t10 model. Compared to *set* 3, *set* 4 models show less ^{12}C fuel available (the ^{12}C abundance is ∼0.075, compared to 0.27 in *set* 3). This is because of the large overlap with the previous convective shell, where most of the carbon fuel was consumed.

Therefore, the relatively low amount of ^{12}C significantly reduces the impact of a higher $^{12}C(^{12}C, n)^{23}Mg$ rate compared with *set* 3, and the average mass fraction is only marginally modified. On the other hand, in the D77t5 case, most of the *r*-only isotopes are increased by a factor of ∼1.2 compared with the standard case, and, at the same time, the *p*-only isotopes are reduced by a similar factor. In fact, such modifications are triggered by local neutron captures due to the final short neutron burst, where *r*-only isotopes are fed from local abundant *s*-process isotopes and the *p*-rich isotopes are more depleted via neutron capture. The impact of a final neutron burst, arising from a higher $^{12}C(^{12}C, n)^{23}Mg$ rate, may be more severe than the case
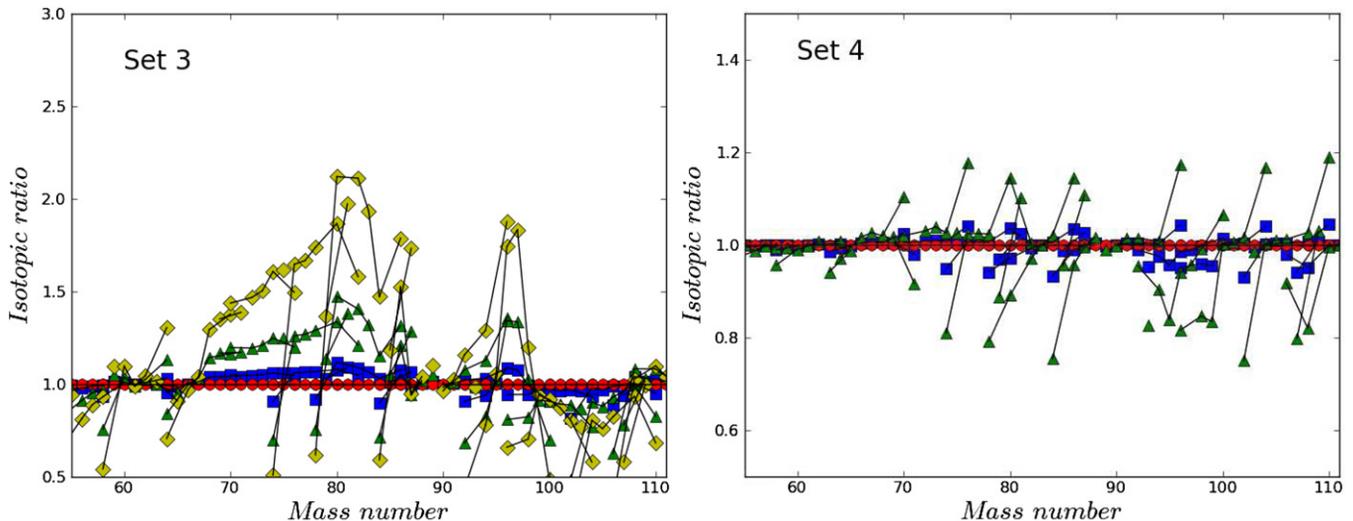
Figure 14. Left panel: the abundances at the end of shell C-burning (when the mass fraction of ^{12}C left is less than 2%) for the *set*3 calculations, using the ^{12}C(^{12}C, n)^{23}Mg rate by Dayras et al. (1977) multiplied by a factor of two (blue squares), by a factor of five (green triangles), and by a factor of 10 (yellow diamonds), normalized to the abundance distribution obtained using the standard ^{12}C(^{12}C, n)^{23}Mg rate. Species belonging to the same element are connected with lines. The temperature and density of these runs are $T = 1.1$ GK and $\rho = 10^5$ g cm^{-3}. Right panel: as in the left panel, but only for the ^{12}C(^{12}C, n)^{23}Mg rate multiplied by 2 (blue squares) and by a factor of five (green triangles). The C shell trajectory used in the calculations is given in Figure 13.

(A color version of this figure is available in the online journal.)

considered in *set*4 since its relevance is directly related to the amount of carbon fuel that is still available when the temperature starts to rise. As such, the estimation regarding the impact of the ^{12}C(^{12}C, n)^{23}Mg uncertainty on C shell yields may change according to the ^{12}C+^{12}C rate used and to the stellar model considered.

Summing up, present *s*-process abundance predictions may be affected locally (at the different branching points producing more *r*-only species, less ^{80}Kr, etc.), and/or more generally over the entire *s*-process distribution, by the uncertainty associated with the ^{12}C+^{12}C neutron channel. Figure 14 shows the two different effects that can be obtained, depending on the stellar model. The ^{12}C(^{12}C, n)^{23}Mg probability needs to be known at stellar carbon burning conditions with a precision significantly better than a factor of five. We have shown that a factor of two precision would have an impact on the *s*-process predictions within an acceptable 10%.

8. IMPLICATIONS FOR THE *p*-PROCESS NUCLEOSYNTHESIS

In this section, we explore the impact of the ^{12}C+^{12}C rate uncertainty on *p*-process nucleosynthesis. In the solar abundance distribution, there are 35 *p*-rich stable nuclei, from ^{74}Se to ^{196}Hg, that are called *p*-only isotopes since they cannot be produced by either the *s*-process or the *r*-process. In the solar system, the *p*-only nuclei are about two orders of magnitude less abundant when compared with the other stable isotopes of the same element fed by the *s*- and *r*-processes. Exceptions are the *p*-nuclei ^{92,94}Mo and ^{96,98}Ru, which represent respectively 14.84, 9.25% and 5.52, 1.88% of the total abundance of the respective element.

Different astrophysical sources have been proposed to either reproduce or contribute to the solar *p*-process distribution (see, e.g., Arnould & Goriely 2003; Fröhlich et al. 2006; Travaglio et al. 2011). At present, the most well-established astrophysical site for *p*-process nucleosynthesis is the O/Ne-rich layers in massive stars, before and after the SN explosion (e.g., Arnould 1976; Woosley & Howard 1978). The pre-explosive

Table 9
As in Table 8, but for *set*4 Cases, Where Calculations Are Based on a Realistic C Shell Trajectory Extracted from the M25CF88t10 Stellar Model

X_i	Mixed He and C Ashes	D77*	D77t5*
C-12	7.555E−02	5.792E−03	5.792E−03
Ne-20	2.791E−01	3.660E−01	3.653E−01
Ne-22	6.701E−04	8.997E−05	9.567E−05
Na-23	1.003E−02	9.882E−03	1.016E−02
Fe-56	1.223E−04	1.120E−04	1.099E−04
Zn-70	5.643E−09	8.376E−09	9.677E−09
Ge-70	3.650E−06	4.156E−06	4.266E−06
Se-76	5.652E−07	6.438E−07	6.648E−07
Kr-80	1.410E−07	6.868E−08	5.936E−08
Kr-82	5.154E−07	4.634E−07	4.445E−07
Sr-88	5.162E−07	5.724E−07	5.843E−07
Y-89	8.285E−08	8.156E−08	8.047E−08
Zr-96	3.718E−10	1.198E−09	1.455E−09
TE-124	9.948E−10	8.840E−10	8.667E−10
Xe-130	1.265E−09	1.199E−09	1.186E−09
Ba-138	2.925E−08	2.999E−08	3.015E−08
msv$_s$	⋯	1.000E+00	9.695E−01

Notes. Note that the case D77t10 is not considered, since the simulations reach higher temperatures where the nuclear uncertainty of the ^{12}C(^{12}C, n)^{23}Mg rate is lower. The symbol * in the labels is used to distinguish from the cases in Table 8, based on different conditions.

p-process component is mostly re-processed by the explosive nucleosynthesis triggered by the SN shock wave. Its effective impact on the total *p*-process yields depends on the explosion mechanism and on the stellar structure behavior in the last days before core collapse. For instance, extensive convection and mixing between different burning shells (e.g., convective O shell mixing with convective C shell; Rauscher et al. 2002) may trigger the enrichment of SN O-rich ejecta by pre-explosive *p*-process nuclei (see also Arnett & Meakin 2011).

Explosive *p*-process nucleosynthesis in standard SNe Type II explosions shows a weak dependence on the initial mass of the star (e.g., Rayet et al. 1995). The initial abundances for the *p*-process are provided by the *s*-process distribution, built in

the previous evolutionary phases. This implies that the p-process efficiency depends on the initial metallicity of the star, showing a secondary nature similar to the weak s-process (Rayet et al. 1995; Arnould & Goriely 2003).

In order to investigate the impact of the ^{12}C+^{12}C rate on the p-process abundances, we have performed a set of one-zone explosive nucleosynthesis simulations. We have used the same explosive trajectories used by Rapp et al. (2006). Initial abundances are given by the pre-explosive composition calculated in the models presented in this paper. In Figure 15 (left panel), we compare the p-process abundance distribution obtained using the abundance seeds from the CF88t10 and CU models (pCF88t10 and pCU, respectively). The other models discussed in the previous sections are similar to pCF88t10 (Section 3). The abundance distribution of pCF88t10 is consistent with previous analyses of the p-process nucleosynthesis in explosive O/Ne layers in massive stars (e.g., Prantzos et al. 1990b; Rayet et al. 1995). About 60% of the p-process isotopes are produced in comparable amounts (e.g., Rayet et al. 1990, 1995). A sample of isotopes is underproduced compared to the average production factor F_0. In all present models, the nuclei ^{92,94}Mo and ^{96,98}Ru are systematically underproduced by an order of magnitude or more in all nucleosynthesis scenarios using realistic massive stars conditions (Arnould & Goriely 2003). This problem cannot be resolved by nuclear physics uncertainties (Rauscher 2006; Rapp et al. 2006). A possible solution was proposed by Arnould et al. (1992), showing that artificially increasing s-process abundances for A $\geqslant$ 90 would solve the Mo–Ru puzzle. It was argued by Costa et al. (2000) that using a larger ^{22}Ne(α, n)^{25}Mg rate (within the upper limit of Angulo et al. 1999) could increase s-process yields in massive stars at the Sr peak and beyond. However, not only is this finding unconfirmed by other results (Heger et al. 2002), such a high rate would also result in disagreement between present weak and main s-process component predictions in the solar system abundance distribution. Furthermore, the capability of the present s-process stellar AGB models to reproduce the s-process signature measured in carbonaceous presolar grains would be called into question (see also discussion in Pignatari et al. 2010).

Alternatively, other processes in massive stars different from the classical p-process have been proposed to contribute to the missing Mo–Ru p abundances, e.g., in α-rich freezout conditions during the SNII explosion (e.g., Hoffman et al. 1996) or the νp process in proton-rich neutrino-wind conditions (Fröhlich et al. 2006). The p-process underproduces ^{113}In and ^{115}Sn within present nuclear uncertainties, despite the potential contribution from the r-process (Rapp et al. 2006; Dillmann et al. 2008, and references therein). On the other hand, ^{152}Gd and ^{164}Er receive a significant contribution from the s-process (e.g., Arlandini et al. 1999; Abbondanno et al. 2004; Best et al. 2001). Finally, ^{138}La might receive a significant contribution from neutrino capture on ^{138}Ba (Goriely et al. 2001), which is not considered in these calculations.

For the pCF88t10 case, we obtain an overproduction of ^{130}Ba, ^{180}Ta, and ^{196}Hg. The overproduction is acceptable within the nuclear uncertainties for ^{130}Ba. The p-process production of ^{180}Ta is affected by the pre-explosive s-process abundance distribution. The pCF88t10 yields presented in Figure 15 are characterized by a general underproduction compared with ^{16}O. According to Rayet et al. (1995), the total production factors for p-nuclei and ^{16}O in the ejected SN material should be comparable, assuming that massive stars are their main astrophysical site. For instance, Rayet et al. (1995) estimated

such underproduction to be at least a factor of two for a 25 $M_\odot$ star, considering uncertainties associated with both the stellar model and nuclear input, such as the ^{12}C(α, γ)^{16}O rate. In the pCF88t10 case, the average overproduction factor is $F_0 = 42.3$.

Considering a mass correction factor of $f_m = 0.2$, the p/O yield ratio is ∼0.12. This takes into account an ^{16}O overproduction factor compared with the solar overabundance (∼70) and the amount of p-rich and O-rich mass ejected by a standard 25 $M_\odot$ core collapse SN model (see for instance Table 3 of Rayet et al. 1995, where f_m ranges from 0.19 to 0.23 depending on the different model prescriptions).

The average overproduction factor of the pCF88t10 case ($F_0 = 42.3$) is consistent with the value provided by Rayet et al. (1995) for a 25 $M_\odot$ model at solar metallicity and for the initial mass function weighted p-process distribution ($F_0 = 130$ and 100, respectively), considering that the classic p-process in massive stars is a secondary process. Indeed, its efficiency critically depends on the s-process abundance seeds from the previous stellar phases (Arnould & Goriely 2003). It is also important to note that according to Tinsley (1980), at solar metallicity secondary species (in this case, the p-process yields) should be produced twice as much as primary species (e.g., ^{16}O). Consequently, the underproduction of the p-process in the SNII scenario is likely to be more severe than mentioned by Rayet et al. (1995); the yield ratio required to reproduce the p-process inventory should be p/O = 2 at solar metallicity, twice as much as previously estimated.

In Figure 15 (left panel), the pCU case shows significant differences compared with the pCF88t10 case. First, F_0 is more than a factor of eight higher than in the standard case ($F_0 = 348$). Second, a good fit is obtained for ^{92,94}Mo and ^{98}Ru within a factor of two uncertainty and only a factor of three underproduction for ^{96}Ru. The higher s-process efficiency of the cs-component in the CU model at the Sr peak and beyond provides the required seed distribution to feed this mass region. It is important to mention that for the pCU case the lighter p-process species are mostly produced by the coldest (and more external) trajectories, whereas in standard p-process conditions they are mostly produced by the hottest (and deepest) particles due to photodisintegration flows destroying heavier species. Therefore, in this case, local photodisintegration channels are mainly responsible for p-nuclei yields, and previous impact studies of nuclear uncertainties (e.g., Rauscher 2006; Rapp et al. 2006) should be reconsidered. The underproduction of ^{113}In, ^{138}La, ^{152}Gd, and ^{164}Er is also confirmed for the pCU case. The problem of ^{130}Ba, ^{180}Ta, and ^{196}Hg overproduction, seen in pCF88t10, is also solved due to the increase of F_0. However, ^{190}Pt is now underproduced.

As a verification test, we compare the pCU p-process abundances with the results obtained by the code used in Rapp et al. (2006), using the same initial distribution and the same trajectories (Figure 15). Considering that the two codes used different nuclear networks, the final compositions are consistent, with maximum yield variation within a factor of two. We also tested how the present results may be affected by using different trajectories. Only marginal variations in the final p-process distribution were obtained by either changing the freezout temperature in the explosive particles, using different power-law prescriptions, or assuming an exponential decrease. Therefore, the present conclusions are not compromised.

From the present calculations, for the higher (CU) ^{12}C+^{12}C rate, the overlap between the convective C core and the convective C shell provides a higher s-process efficiency at the Sr
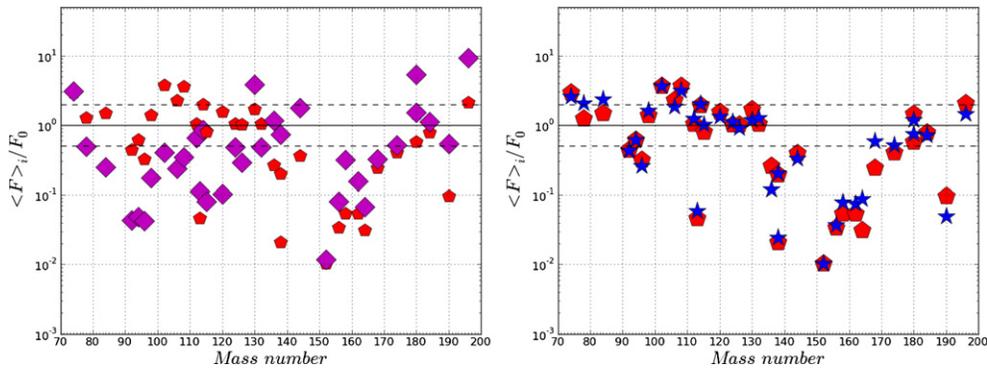
Figure 15. Left panel: average overabundance distribution of the *p*-process nuclei over the 14 trajectories by Rapp et al. (2006), for the 25 $M_\odot$ star, $Z = 0.01$, using as seeds the abundances from the CF88t10 model (pCF88t10, purple diamonds) and CU (pCU, red pentagons). The average overproduction factor F_0 is 42.3 and 347.7, respectively. Right panel: the pCU distribution is compared with the same case, calculated using the post-processing code by Rapp et al. (2006).

(A color version of this figure is available in the online journal.)

peak and beyond, forming the *cs*-component (Section 5). Such a distribution feeds enhanced *p*-process yields, also reproducing the solar *p*-process abundances in the Mo–Ru region within a factor of 2–3 (Figure 15). Therefore, the *cs*-component obtained from the CU model provides a set of *s*-process seeds that may efficiently feed the final abundances of the puzzling Mo and Ru *p*-only species, and provide a satisfactory distribution of heavier *p*-nuclei.

We have seen that the *cs*-component is difficult to reconcile with the *s*-process abundances observed in the solar system, unless only a few per cent of the total *s*-process-rich mass ejected by massive stars can carry it. By extension, the *p*-process-rich distribution obtained from CU (*cp*-component, hereafter) has to follow the same restrictions as discussed in Section 5. Indeed, we have shown that if about 2% of the *s*-process-rich mass ejected into the interstellar medium has the enhanced component, then this could provide a possible scenario to solve the LEPP puzzle in the solar system distribution. Assuming that 2% of the ejected *p*-process-rich mass carries the *cp*-component (with $F_0 = 348$ in the pCU case), only about 2% of the average *p*-process abundance in the solar system distribution could be reproduced by the *cp*-component ($348 \times f_m \times 0.02/70$, where $f_m = 0.2$ is the mass correction factor described above and 70 is the ^{16}O overproduction). The F_0 from the pCF88t10 case, assuming that the remaining ejected mass shows a standard *s*-process and *p*-process signature, would correspond to ∼12% of the average *p*-process solar distribution. The low *p*-process efficiency in massive stars simulations cannot therefore be solved by considering the *cp*-component in the *p*-process inventory, and it is even worse than previously estimated if we also consider the secondary nature of the classic *p*-process. An amount of only a few per cent of solar Mo–Ru *p*-nuclei could be produced. If such speculations will be confirmed, another astrophysical source for the cosmic abundances of the *p*-process nuclei is needed. In this direction, thermonuclear supernovae (SNeIa) might efficiently produce *p*-process abundances in their ejecta (Howard et al. 1991; Howard & Meyer 1993; Kusakabe et al. 2011; Travaglio et al. 2011). In particular, Travaglio et al. (2011) provide SN Ia simulations where a relevant fraction of the *p*-process abundances in the solar system inventory are reproduced.

These final considerations however are based on only one stellar mass, and the trajectories used for the *p*-process calculations are based on one-zone SN explosion trajectories (Rapp et al. 2006). Recent calculations have shown that fall-back in core-collapse SNe could actually drastically reduce the amount of

O-rich mass ejected for stars with masses heavier than ∼20 $M_\odot$ (Fryer et al. 2009). The impact of this on final *p*-process yields still needs to be estimated in detail, and for different masses. One possible implication is that *p*-process yields may depend on which SN engine is considered. Nevertheless, the intriguing scenario where part of the missing LEPP component may be related to the missing *p*-process abundances of Mo and Ru, and more in general with a new component for the *p*-process inventory, can be constrained or ruled out by an experimental measurement of the ^{12}C+^{12}C rate at stellar temperatures.

9. IMPLICATIONS FOR THE *s*-PROCESS NUCLEOSYNTHESIS AT LOW METALLICITY

In previous sections, the impact of the ^{12}C+^{12}C rate uncertainty on *s*- and *p*-process nucleosynthesis near solar metallicity has been analyzed. In this section, we discuss the implications for the *s*-process at low metallicity. In Section 5, we showed that the *cs*-process may at least partially contribute to the LEPP component in the solar system. Travaglio et al. (2004) proposed that the solar LEPP component is due to a primary process already active in the early universe, leaving a signature that has been observed in the Galactic halo for Sr, Y, and Zr (e.g., Truran et al. 2002). Whether the "solar" LEPP and the "stellar" LEPP (see definitions and discussion in Montes et al. 2007) are either the same process or due to a combination of different processes is still matter of debate. More observations involving Sr–Y–Zr and other elements in the LEPP mass region (from the Sr peak up to Te–Xe) are required in order to shed more light into the origin of LEPP (Farouqi et al. 2009; Chiappini et al. 2011; Hansen & Primas 2011). Following the analysis of the previous sections, one possible question is: Can the *cs*-process efficiently contribute to the so-called stellar LEPP at low metallicity?

Another efficient *s*-process component has been proposed, occurring in fast rotating stars of low metallicity (Pignatari et al. 2008; Frischknecht et al. 2012). This component is triggered by the production of primary ^{22}Ne and the consequent activation of ^{22}Ne$(\alpha, n)^{25}$Mg. Since, in principle, the *cs*-process may also be produced and ejected by fast rotating massive stars, what is the impact on the *s*-process ejecta of these two combined components? Stellar evolution models including the effects of rotation are successful in reproducing several observations, like nitrogen chemical enrichment in the early Galaxy (Heger & Langer 2000; Meynet & Maeder 2000) or the ratio of Wolf–Rayet to O-type stars (Vázquez et al. 2007; Frischknecht et al. 2010, and reference therein).
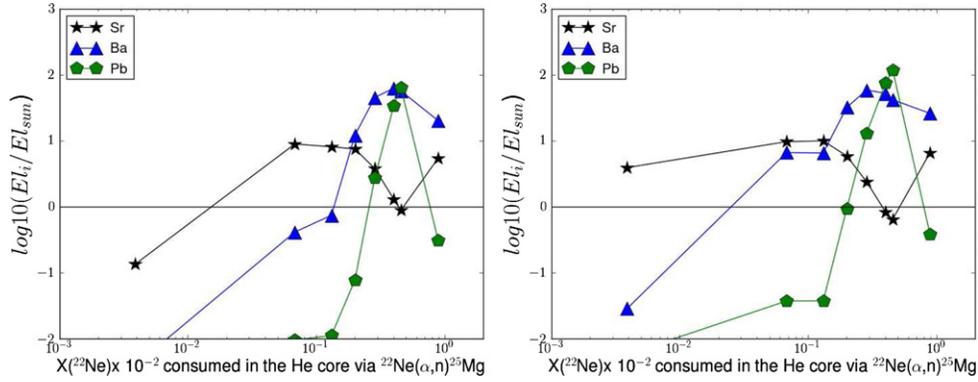
Figure 16. Left panel: the element abundances for Sr, Y, Zr, Ba, and Pb are given at the end of C-burning for different sets of initial compositions, taken from the He core ashes where different amount of primary ^{22}Ne is available and consumed by the ^{22}Ne$(\alpha, n)^{25}$Mg (25 $M_\odot$ star, [Fe/H] = −3; Pignatari et al. 2008). The ^{12}C+^{12}C rate used is CF88; temperature and density are $T = 1.0$ GK and $\rho = 10^5$ cm^{-3} (set 1b). Right panel: as the left panel, but for $T = 0.65$ GK and $\rho = 10^4$ g cm^{-3}, and using the CU ^{12}C+^{12}C rate (set 2b).

(A color version of this figure is available in the online journal.)

There are, however, some unresolved issues in rotating models. A more efficient breaking mechanism is necessary to explain the rotation rates of white dwarfs and millisecond pulsars. Although magnetic fields help, it is not clear yet whether their effect is sufficient (Suijs et al. 2008). Rotation-induced shear mixing at the envelope–core interface in AGB stars may be too strong and thus disable the s-process via radiative ^{13}C-burning in the interpulse phase of low-mass AGB stars (Herwig et al. 2003; Siess et al. 2004). Keeping this in mind, the cs-process behavior with metallicity does not depend on rotation-induced mixing, and the s-process component in fast rotators mentioned above is a realistic scenario to consider within the uncertainties of the present models.

We have performed a set of calculations at [Fe/H] = −3. Stars with this metallicity showing the LEPP component are observed in the Galactic halo (e.g., HD 122563 at [Fe/H] = −2.7; Honda et al. 2006). A set of different initial abundances were taken from Pignatari et al. (2008), at the end of convective core He-burning, considering a large spread of primary ^{22}Ne available in the He core due to rotational mixing. Two different C-burning trajectories were used in the simulations: a set 1 trajectory (Section 6, $T = 1.0$ GK, $\rho = 10^5$ g cm^{-3}, using the CF88 ^{12}C+^{12}C rate, hereafter set 1b), which reproduced C shell conditions without the cs-process component, and a set 2 trajectory (Section 6, $T = 0.65$ GK, $\rho = 10^4$ g cm^{-3}, using the CU ^{12}C+^{12}C rate, hereinafter set 2b), which did include the cs-process component. For complete fast rotating stellar model calculations at different metallicities, we refer to Frischknecht et al. (2012). In Figure 16 (left panel), the production of elements located at the various neutron magic peaks is shown for set 1b for different initial abundance distributions, defined by the amount of ^{22}Ne that is consumed by ^{22}Ne$(\alpha, n)^{25}$Mg in the previous He core phase (^{22}Ne$_{\text{burnt}}$). The first case at ^{22}Ne$_{\text{burnt}} \sim 4 \times 10^{-5}$ uses an abundance distribution from a non-rotating star, where the available ^{22}Ne comes only from the initial CNO abundances at [Fe/H] = −3, considering also the α-enhancement at this metallicity. The other cases have initial abundances with an enhanced s-process distribution, due to the primary ^{22}Ne neutron source being activated in fast rotating massive stars (Pignatari et al. 2008). In particular, the test at ^{22}Ne$_{\text{burnt}} \sim 2 \times 10^{-3}$ corresponds to the standard case considered at [Fe/H] = −3 in Pignatari et al. (2008, with the primary ^{22}Ne around 1% by mass in the He core). We also used as initial distributions unpublished results obtained from the same study, where different amounts

of primary ^{22}Ne were available in the He core. The cases with ^{22}Ne$_{\text{burnt}} \sim 4 \times 10^{-3}$ correspond to ~2% of available primary ^{22}Ne. Finally, we also included an extreme case, where about 1% of ^{22}Ne is burnt by the ^{22}Ne$(\alpha, n)^{25}$Mg in the He core.

As already mentioned by Pignatari et al. (2008), in set 1b most of the s-process yields are produced in the core He-burning phase, and only a partial modification occurs in the later shell C-burning phase. Production of the Sr–Y–Zr peak is robust over a large range of primary ^{22}Ne$_{\text{burnt}}$ (~7 × 10^{-4}–3 × 10^{-3}). Above 3 × 10^{-3}, material at the Sr peak starts to be depleted, feeding heavier elements along the s-process path. For ^{22}Ne$_{\text{burnt}} \sim 2 \times 10^{-3}$ Ba starts rising, as well as Pb for ^{22}Ne$_{\text{burnt}} \sim 3 \times 10^{-3}$. At ^{22}Ne$_{\text{burnt}} \sim 5 \times 10^{-3}$, Ba and Pb productions reach their largest abundance. Increasing the amount of ^{22}Ne$_{\text{burnt}}$ to ~10^{-2} causes the Sr peak material to rise again, whereas Ba and Pb decrease. To burn 1% of ^{22}Ne via ^{22}Ne$(\alpha, n)^{25}$Mg requires that the amount of primary ^{22}Ne is 5% or more. Such a large abundance would make ^{22}Ne acting mostly as a neutron poison, consuming the neutrons produced. Indeed, the production of Ba and Pb is limited not only by the amount of iron seeds available, but also by the dual neutron source/neutron poison nature of ^{22}Ne. Note that, however, such an amount of ^{22}Ne is a significant overestimate from present predictions of fast rotating massive stars (Meynet et al. 2006; Hirschi et al. 2008; Frischknecht et al. 2012). Interestingly, this last case is different from AGB stars at low metallicity, where ^{22}Ne becomes both a seed and a poison for s-process nucleosynthesis up to lead. In the AGB case, the main neutron source is the ^{13}C$(\alpha, n)^{16}$O reaction and the neutron exposure is high enough to produce heavy elements starting from light species (Gallino et al. 2006).

In Figure 16 (right panel), we show the same calculations for set 2b, where the cs-process contribution has also been considered, due to the activation of ^{13}C$(\alpha, n)^{16}$O. Compared with the abundance at the He core exhaustion for the non-rotating case, the Sr production factor compared with solar increases by about 40 times, up to 3.9. Production factors of Ba and Pb increase by about 5 and 2 times, up to 0.028 and 0.006, respectively. At both solar-like and [Fe/H] = −3 metallicities, the bulk of s-process production is found at the Sr peak, with minor contributions to heavier elements. If we compare the Sr production factor obtained here and the one obtained with the M25CU model and half-metallicity (Table 6), a secondary-like trend with the initial composition is observed, while light neutron poisons are mostly primary. Consequently,

the iron seeds force the nature of this *s*-process component to be secondary, just like the *s*-process in fast rotators.

Concerning fast rotating massive stars, the production of Sr–Y–Zr is not affected much by the *cs*-process component. In fact, the production of Sr has almost been saturated during the previous core He−burning phase, since most of the Fe seeds have already been consumed (Pignatari et al. 2008; Frischknecht et al. 2012). As a result, the Sr–Y–Zr *s*-process yields from fast rotating massive stars are robust over a large range of $^{22}Ne_{burnt}$ (i.e., the spread of initial stellar mass and the efficiency of rotation-induced mixing), within nuclear uncertainties of critical reaction rates like $^{22}Ne+\alpha$ (Pignatari et al. 2008), $^{17}O(\alpha, \gamma)^{21}Ne$ (Hirschi et al. 2008), and $^{12}C+^{12}C$. However, relevant uncertainties may be associated with other nuclear reactions not considered here, and with the treatment of rotation in stars.

The production of Ba and Pb is boosted by the *cs*-process, which eventually feeds the Pb peak more efficiently for larger values of $^{22}Ne_{burnt}$. Indeed comparing results from *set* 1*b* and *set* 2*b*, Figure 16, shows that the maximum production factors of Sr–Y–Zr and Ba are similar, whereas Pb is produced by a factor of two more in *set* 2*b*. Additionally, in *set* 2*b* calculations, ^{22}Ne is only partially destroyed and also behaves like an efficient neutron poison. Therefore, the more primary ^{22}Ne (and $^{25,26}Mg$, direct products via α capture on ^{22}Ne) there is available in the He core ashes, the less efficiently the *cs*-process feeds the heavier elements. In general, the maximum elemental ratio Pb/Ba that can be produced in the present calculations for fast rotating massive stars is ∼3, including the uncertainty related to the amount of primary ^{22}Ne available and/or consumed by the $^{22}Ne(\alpha, n)^{25}Mg$, as well as the uncertainty in the $^{12}C+^{12}C$ rate. Taking into account the present $^{22}Ne(\alpha, n)^{25}Mg$ uncertainty, such conditions can be obtained when the primary ^{22}Ne abundance in the He core is about 2% for a 25 $M_{\odot}$ star (about a factor of two more than predicted by Hirschi et al. 2008), or for stars with larger initial mass, where ^{22}Ne depletion via α-capture is more efficient. According to stellar model calculations by Hirschi et al. (2008), the production factors of Sr, Ba, and Pb are 7.5, 12.0, and 0.08, respectively, becoming 5.9, 31.9, and 0.9 when the contribution from the *cs*-process is included (Figure 16). In this case, therefore, *s*-process elements are efficiently produced only up to Ba, also taking into account the $^{12}C+^{12}C$ uncertainty.

In Pignatari et al. (2008), it was shown that the *s*-process in fast rotating massive stars due to primary ^{22}Ne is a secondary process. This was confirmed by similar results obtained for a complete set of fast rotating stellar models (Frischknecht et al. 2012). As discussed before, the *cs*-process is also secondary-like. In Section 5, it was shown that in principle the *cs*-component is a possible scenario for explaining the LEPP in the solar system without failing the weak *s*-process distribution. Assuming that the same constraints discussed in Section 5 are also valid for low metallicity, only a few massive stars would eject such a component at [Fe/H] $\lesssim -3$.

The LEPP signature could have been observed in stars such as HE 1327−2326, where [Fe/H] = −5.45 (Frebel et al. 2005), for which the efficiency of the *cs*-process compared with other primary explosive processes in massive stars proposed to feed the Sr–Y–Zr peak is supposed to be lower (Woosley & Hoffman 1992; Qian & Wasserburg 2007; Farouqi et al. 2008; Arcones & Montes 2011). However, because at present only the upper limits of Ba and Eu are available for this star, whether or not HE 1327−2326 is an LEPP star still requires confirmation. A detailed comparison between stellar yields and spectroscopic

observations of metal-poor LEPP stars is beyond the scope of this paper, since complete massive stellar calculations at low metallicity would be required.

In fast rotating massive stars, the occurrence of the *cs*-process would not affect the conclusions of Pignatari et al. (2008) concerning nucleosynthesis at the Sr–Y–Zr peak. If such a component does exist however, a more efficient production of Sr–Y–Zr is obtained also at lower rotation efficiencies, and for fast rotators Ba peak elements, and possibly Pb, could be more abundant in the final *s*-process yields. The present calculations explored the possible impact of the $^{12}C+^{12}C$ rate uncertainty on the *s*-process at low metallicity, in non-rotating and fast rotating stars. The analysis presented in this section is based on one-zone nucleosynthesis calculations and not on full stellar models. However, we did use realistic stellar conditions and explored the impact of various uncertainties on theoretical abundance predictions, which provides some guidance about *s*-process nucleosynthesis in massive stars at low metallicity. In the case that future nuclear physics experiments suggest a higher $^{12}C+^{12}C$ rate than the CF88 rate for central C-burning conditions, a new set of complete stellar models at low metallicity and different rotation efficiencies would be required in order to revise the present estimates of *s*-process nucleosynthesis stellar yields in the early universe.

10. CONCLUSIONS

The aim of the present work was to explore the impact of the $^{12}C+^{12}C$ rate uncertainty in massive stars, on pre-SN nucleosynthesis, and on the explosive *p*-process. Our analysis was focused on one mass and metallicity (25 $M_{\odot}$ and half solar metallicity) and considered a large variation of the $^{12}C+^{12}C$ rate: the lower rate limit took into account possible hindrance effects in the carbon fusion reaction, whereas the upper limit considered contributions from potential subthreshold resonances at low temperature.

In all, we considered five different $^{12}C+^{12}C$ rates: the lower limit (CL), the standard rate of CF88, CF88 divided and multiplied by a factor of 10 (CF88d10 and CF88t10, respectively), and the upper limit (CU). Other reactions critical for the energy generation during stellar evolution were left unchanged. Up to central He exhaustion, the five stellar models obtained with these rates (M25CL, M25CF88d10, M25CF88, M25CF88t10, and M25CU) share the same conditions.

With the lower $^{12}C+^{12}C$ rates, CL and CF88d10, the *s*-process during convective shell C-burning shows a slightly lower neutron exposure, coupled with a higher neutron density peak, causing local effects at the branching points along the *s*-process path (e.g., ^{79}Se and ^{85}Kr). The production of long-lived isotopes ^{26}Al and ^{60}Fe during the pre-explosive phase is also affected, as discussed by Gasques et al. (2007). In particular, we confirm that ^{60}Fe tends to be produced more with lower $^{12}C+^{12}C$ rates. However, results for ^{26}Al are strongly affected by the stellar model used. In fact, if the convective C shell is switched off before the core collapse starts, all of the ^{26}Al has the time to decay. As a result, the final stellar yields only contain explosive ^{26}Al. The model with the highest pre-explosive ^{26}Al abundance in the C shell material is M25CF88t10, since it is the only one to keep a convective C shell until core collapse. Because the pre-explosive component of ^{26}Al is model dependent, the final $^{26}Al/^{60}Fe$ in SN ejecta needs to be regarded cautiously.

For the higher $^{12}C+^{12}C$ rates, CF88t10 and CU, the final *s*-process yields tend to increase toward the Sr peak with respect

to lighter s-process elements. In the M25CF88t10 model, such an increase is within 20%, depending on the isotope considered, and is due to the overlap between the first shell and the second convective carbon shell (Bennett et al. 2010). In the M25CU model, the activation of $^{13}C(\alpha, n)^{16}O$ in the C core causes the formation of the cs-process component, which will also dominate the final C shell ejecta. In agreement with Paper I, the s-process yields at the Sr peak increase by about two orders of magnitude. It was shown that if only $\sim$2% of the s-process-rich material from massive stars carries the cs-process signature, the weak s-process component from other stars would not be affected and the cs-process could reproduce at least part of the LEPP component in the solar system.

We have provided a series of tests in which the strengths to the two dominant nucleosynthesis channels of the carbon-fusion reactions $^{12}C(^{12}C, \alpha)^{20}Ne$ and $^{12}C(^{12}C, p)^{23}Na$ have been changed. The impact of using a different R_α/R_p ratio changes according to the total $^{12}C+^{12}C$ rate. For the calculations using CF88, the amount of neutrons available (and the s-process efficiency) decreases with increasing proton channel strength compared to the α channel. Indeed, ^{22}Ne depletion in C-burning conditions is dominated by the (α, n) and (p, γ) channels, which are respectively affected by the amount of α and protons available. The cs-process, on the other hand, drastically loses its efficiency with increasing α channel strength, because less protons are available to produce ^{13}C via $^{12}C(p, \gamma)^{13}N(\beta^+)^{13}C$. For instance, using a ratio $R_\alpha/R_p = 0.95/0.05$ (10 times higher than the standard $R_\alpha/R_p = 0.65/0.35$), the Sr abundance decreases by about a factor of 30. Small variations are obtained from reducing the α channel strength. Critical light species are also affected by R_α/R_p using the CU $^{12}C+^{12}C$ rate: ^{16}O and ^{23}Na decrease with a high R_α/R_p ratio, while ^{20}Ne increases. Therefore, uncertainty in the R_α/R_p ratio may affect abundances of species that are the main fuel for following evolutionary phases.

We also tested the impact of the uncertainty of the channel $^{12}C(^{12}C, n)^{23}Mg$ on the s-process calculations, assuming a range of probability between the standard rate (D77) and D77 multiplied by 10 (D77t10). First of all, the impact of the neutron channel increases with increasing amounts of ^{12}C available at the onset of shell C-burning. This in turn may depend on the $^{12}C(\alpha, \gamma)^{16}O$ rate during the previous core He-burning and convection prescription, as well as the total $^{12}C+^{12}C$ rate. In the simulations reproducing the typical C shell conditions using the CF88 $^{12}C+^{12}C$ rate, it was seen that the neutron channel uncertainty causes a propagation effect in the s-process distribution, peaked at the s-only isotopes $^{80,82}Kr$, with an increase of more than a factor of two. On the other hand, in the last convective C shell of the M25CF88t10 model, uncertainty in the neutron channel only becomes important in the final phase, associated with a temperature and density rise, when the higher neutron density (being driven mostly by $^{12}C(^{12}C, n)^{23}Mg$) increases the abundance of the r-only isotopes (e.g., ^{70}Zn and ^{76}Se) by 20%–30%.

We have studied the impact of the $^{12}C+^{12}C$ rate uncertainty on the p-process yields, using standard p-process trajectories from SN explosion (Rapp et al. 2006). In particular, with the exception of the M25CU yields, the p-process calculations show comparable results. The cs-process component feeds the production of extremely abundant p-process yields (cp-process), with average p-only abundance 8.3 times higher than the standard p-process, and also reproducing the Mo and Ru p-only abundances. GCE calculations based on stellar models

of different masses and using updated SN explosions would be required to study the impact of the cp-process on the chemical inventory of the p nuclei.

Finally, we have explored the possible impact of the $^{12}C+^{12}C$ rate for non-rotating and fast-rotating massive stars with low metallicity ([Fe/H] $= -3$). It was found that at the considered metallicity the cs-process is secondary, despite the primary neutron source $^{13}C(\alpha, n)^{16}O$ and mainly primary neutron poisons. The possible existence of the of the cs-component does not modify previous conclusions regarding the s-process in fast rotating massive stars, due to the primary ^{22}Ne neutron source. The main effects of the cs-process are a relevant abundance production at the Sr peak, even without rotation, and the production of elements heavier than Sr–Y–Zr, up to the Ba peak and eventually up to Pb, in fast rotating massive stars. However, an efficient production of lead would occur for concentrations of primary ^{22}Ne in the He core that are a factor of two higher than have previously been considered (see for more details Pignatari et al. 2008). Considering the cs-process contribution or, in other words, the $^{12}C+^{12}C$ rate uncertainty, a maximum ratio of Pb/Ba ~ 3 was estimated for the s-process yields. The production of more Pb compared with other lighter elements is limited by the amount of primary ^{22}Ne. If there is too much of it available in the He core, then its neutron poison efficiency reduces the s-process beyond iron, or alternatively a $^{22}Ne(\alpha, n)^{25}Mg$ rate higher than the present uncertainty would be required.

REFERENCES

Abbondanno, U., Aerts, G., Alvarez-Velarde, F., et al. 2004, PhRvL, 93, 161103
Abegg, R., & Davis, C. A. 1991, PhRvC, 43, 2523
Aikawa, M., Arnould, M., Goriely, S., Jorissen, A., & Takahashi, K. 2005, A&A, 441, 1195
Anders, E., & Grevesse, N. 1989, GeCoA, 53, 197
Angulo, C., Arnould, M., Rayet, M., et al. 1999, NuPhA, 656, 3
Arcones, A., & Montes, F. 2011, ApJ, 731, 5
Arlandini, C., Käppeler, F., Wisshak, K., et al. 1999, ApJ, 525, 886
Arnett, W. D. 1972, ApJ, 176, 699
Arnett, W. D. 1974, ApJ, 194, 373
Arnett, W. D., & Meakin, C. 2011, ApJ, 733, 78
Arnett, W. D., & Thielemann, F.-K. 1985, ApJ, 295, 589
Arnett, W. D., & Truran, J. W. 1969, ApJ, 157, 339
Arnett, W. D., & Wefel, J. P. 1978, ApJL, 224, 139
Arnould, M. 1976, A&A, 46, 117
Arnould, M., & Goriely, S. 2003, PhR, 384, 1
Arnould, M., Rayet, M., & Hashimoto, M. 1992, in Unstable Nuclei in Astrophysics, ed. S. Kubono & T. Kajino (Singapore: World Scientific), 23
Baraffe, I., El Eid, M. F., & Prantzos, N. 1992, A&A, 258, 357
Becker, H. W., Kettner, K. U., Rolfs, C., & Trautvetter, H. P. 1981, ZPhyA, 303, 305
Bennett, M. E., Hirschi, R., Pignatari, M., et al. 2010, in Nuclei in the Cosmos XI (Trieste: SISSA), PoS (NIC XI) 182

Bennett, M. E., Hirschi, R., Pignatari, M., et al. 2012, MNRAS, 420, 3047
Best, J., Stoll, H., Arlandini, C., et al. 2001, PhRvC, 64, 015801
Bromley, D. A., Kuehner, J. A., & Almqvist, E. 1960, PhRvL, 4, 365
Caughlan, G. R., & Fowler, W. A. 1988, ADNDT, 40, 283
Chiappini, C., Frischknecht, U., Meynet, G., et al. 2011, Natur, 472, 454
Chieffi, A., Limongi, M., & Straniero, O. 1998, ApJ, 502, 737
Clayton, D. D. 1968, Principles of Stellar Evolution and Nucleosynthesis (New York: McGraw-Hill)
Coquard, L., Käppeler, Dillmann, I., et al. 2006, in Nuclei in the Cosmos IX (Trieste: SISSA), PoS (NIC IX) 274
Costa, V., Rayet, M., Zappalà, R. A., & Arnould, M. 2000, A&A, 358, L67
Couch, R. G., Schmiedekamp, A. B., & Arnett, W. D. 1974, ApJ, 190, 95
Davis, C. A. 1981, PhRvC, 24, 1891
Dayras, R., Switkowski, Z. E., & Woosley, S. E. 1977, NuPhA, 279, 70
de Jager, C., Nieuwenhuijzen, H., & van der Hucht, K. A. 1988, A&AS, 72, 259
Dillmann, I., Heil, M., Käppeler, F., et al. 2006, in AIP Conf. Proc.819, ed. A. Woehr & A. Aprahamian (Melville, NY: AIP), 123
Dillmann, I., Käppeler, F., Rauscher, T., et al. 2008, in Nuclei in the Cosmos X (Trieste: SISSA), PoS (NIC X) 091
Eggenberger, P., Meynet, G., Maeder, A., et al. 2008, Ap&SS, 316, 43
El Eid, M. F., Meyer, B. S., & The, L.-S. 2004, ApJ, 611, 452
El Eid, M. F., The, L.-S., & Meyer, B. S. 2009, SSRv, 34
Endt, P. 1990, NuPhA, 521, 1
Farouqi, K., Kratz, K.-L., Cowan, J. J., et al. 2008, in AIP Conf. Proc.990, First Stars III, ed. B. W. O'Shea & A. Heger (Melville, NY: AIP), 309
Farouqi, K., Kratz, K.-L., Mashonkina, L. I., et al. 2009, ApJL, 694, 49
Farouqi, K., Kratz, K.-L., Pfeiffer, B., et al. 2010, ApJ, 712, 1359
Ferguson, J. W., Alexander, D. R., Allard, F., et al. 2005, ApJ, 623, 585
Ford, J. L. C., Jr., Gomez Del Campo, J., Robinson, R. L., Stelson, P. H., & Thornton, S. T. 1974, NuPhA, 226, 189
Fowler, W. A., Caughlan, G. R., & Zimmerman, B. A. 1975, ARA&A, 13, 69
Frebel, A., Aoki, W., Christlieb, N., et al. 2005, Natur, 434, 871
Freer, M. 2007, RPPh, 70, 2149
Frischknecht, U., Hirschi, R., Meynet, G., et al. 2010, A&A, 522, A39
Frischknecht, U., Hirschi, R., & Thielemann, F.-K. 2012, A&A, 538, L2
Fröhlich, C., Hix, W. R., Martínez-Pinedo, G., et al. 2006, NewAR, 50, 496
Fryer, C. L., Brown, P. J., Bufano, F., et al. 2009, ApJ, 707, 193
Fuller, G. M., Fowler, W. A., & Newman, M. J. 1985, ApJ, 293, 1
Fynbo, H. O. U., Diget, C. A., Bergmann, U. C., et al. 2005, Natur, 433, 136
Gallino, R., Arlandini, C., Busso, M., et al. 1998, ApJ, 497, 388
Gallino, R., Bisterzo, S., Husti, L., et al. 2006, in Nuclei in the Cosmos IX (Trieste: SISSA), PoS (NIC XI) 100
Gasques, L. R., Afanasjev, A. V., Aguilera, E. F., et al. 2005, PhRvC, 72, 025806
Gasques, L. R., Brown, E. F., Chieffi, A., et al. 2007, PhRvC, 76, 035802
Goriely, S., Arnould, M., Borzov, I., & Rayet, M. 2001, A&A, 375, L35
Hansen, C. J., & Primas, F. 2011, A&A, 525, L5
Heger, A., & Langer, N. 2000, ApJ, 544, 1016
Heger, A., Woosley, S. E., Rauscher, T., Hoffman, R. D., & Boyes, M. M. 2002, NewAR, 46, 463
Herwig, F., Diehl, S., Fryer, C. L., et al. 2008, in Nuclei in the Cosmos X (Trieste: SISSA), PoS (NIC X) 023
Herwig, F., Langer, N., & Lugaro, M. 2003, ApJ, 593, 1056
High, M. D., & Čujec, B. 1977, NuPhA, 282, 181
Hirschi, R., Frischknecht, U., Pignatari, M., et al. 2008, in Nuclei in the Cosmos X (Trieste: SISSA), PoS (NIC X) 083
Hirschi, R., Meynet, G., & Maeder, A. 2004, A&A, 425, 649
Hoffman, R. D., Woosley, S. E., Fuller, G. M., & Meyer, B. S. 1996, ApJ, 460, 478
Honda, S., Aoki, W., Ishimaru, Y., Wanajo, S., & Ryan, S. G. 2006, ApJ, 643, 1180
Howard, W. M., & Meyer, B. S. 1993, in Proc. of the 2nd International Symposium on Nuclear Astrophysics, Nuclei in the Cosmos, ed. F. Käppeler & K. Wisshak (Bristol: Institute of Physics Publishing), 575
Howard, W. M., Meyer, B. S., & Woosley, S. E. 1991, ApJL, 373, 5
Imbriani, G., Costantini, H., Formicola, A., et al. 2005, EPJA, 25, 455
Imbriani, G., Limongi, M., Gialanella, L., et al. 2001, ApJ, 558, 903
Itoh, N., Hayashi, H., Nishikawa, A., & Kohyama, Y. 1996, ApJS, 102, 411
Jaeger, M., Kunz, R., Mayer, A., et al. 2001, PhRvL, 87, 202501
Jiang, C. L., Back, B. B., Esbensen, H., et al. 2008, PhRvC, 78, 017601
Jiang, C. L., Rehm, K. E., Back, B. B., & Janssens, R. V. F. 2007, PhRvC, 75, 015803
Käppeler, F., Beer, H., & Wisshak, K. 1989, RPPh, 52, 945
Käppeler, F., Beer, H., Wisshak, K., et al. 1982, ApJ, 257, 821
Käppeler, F., Wiescher, M., Giesen, U., et al. 1994, ApJ, 437, 396

Kettner, K. U., Lorenz-Wirzba, H., & Rolfs, C. 1980, ZPhyA, 298, 65
Kunz, R., Fey, M., Jaeger, M., et al. 2002, ApJ, 567, 643
Kusakabe, M., Iwamoto, N., & Nomoto, K. 2011, ApJ, 726, 25
Lamb, S. A., Howard, W. M., Truran, J. W., & Iben, I., Jr. 1977, ApJ, 217, 213
Langanke, K., & Martínez-Pinedo, G. 2000, NuPhA, 673, 481
Limongi, M., & Chieffi, A. 2006, ApJ, 647, 483
Limongi, M., Straniero, O., & Chieffi, A. 2000, ApJS, 129, 625
Lodders, K. 2003, ApJ, 591, 1220
Maeder, A. 1992, A&A, 264, 105
Mazarakis, M. G., & Stephens, W. E. 1973, PhRvC, 7, 1280
McDonald, A., Earle, E., McLatchie, W., et al. 1978, NuPhA, 305, 151
McGrath, R. L., Cerny, J., Hardy, J. C., Goth, G., & Arima, A. 1970, PhRvC, 1, 184
Meynet, G., Ekström, S., & Maeder, A. 2006, A&A, 447, 623
Meynet, G., & Maeder, A. 2000, A&A, 361, 101
Mişicu, Ş., & Esbensen, H. 2006, PhRvL, 96, 112701
Montes, F., Beers, T. C., Cowan, J., et al. 2007, ApJ, 671, 1685
Mukhamedzhanov, A. M., Bém, P., Brown, B. A., et al. 2003, PhRvC, 67, 065804
Nomoto, K., Tominaga, N., Umeda, H., Kobayashi, C., & Maeda, K. 2006, NuPhA, 777, 424
Oda, T., Hino, M., Muto, K., Takahara, M., & Sato, K. 1994, ADNDT, 56, 231
Patterson, J. R., Winkler, H., & Zaidins, C. S. 1969, ApJ, 157, 367
Perez-Torres, R., Belyaeva, T., & Aguilera, E. 2006, PAN, 69, 1372
Peters, J. G. 1968, ApJ, 154, 225
Pignatari, M., & Gallino, R. 2008, in AIP Conf. Proc.990, First Stars III, ed. B. W. O'Shea & A. Heger (Melville, NY: AIP), 336
Pignatari, M., Gallino, R., Heil, M., et al. 2010, ApJ, 710, 1557
Pignatari, M., Gallino, R., Meynet, G., et al. 2008, ApJL, 687, 95
Prantzos, N., Hashimoto, M., & Nomoto, K. 1990a, A&A, 234, 211
Prantzos, N., Hashimoto, M., Rayet, M., & Arnould, M. 1990b, A&A, 238, 455
Qian, Y.-Z., & Wasserburg, G. J. 2007, PhR, 442, 237
Raiteri, C. M., Busso, M., Picchio, G., & Gallino, R. 1991a, ApJ, 371, 665
Raiteri, C. M., Busso, M., Picchio, G., Gallino, R., & Pulone, L. 1991b, ApJ, 367, 228
Raiteri, C. M., Gallino, R., & Busso, M. 1992, ApJ, 387, 263
Raiteri, C. M., Gallino, R., Busso, M., Neuberger, D., & Käppeler, F. 1993, ApJ, 419, 207
Rapp, W., Görres, J., Wiescher, M., Schatz, H., & Käppeler, F. 2006, ApJ, 653, 474
Rauscher, T. 2006, PhRvC, 73, 015804
Rauscher, T., Heger, A., Hoffman, R. D., & Woosley, S. E. 2002, ApJ, 576, 323
Rauscher, T., & Thielemann, F.-K. 2000, ADNDT, 75, 1
Rayet, M., Arnould, M., Hashimoto, M., Prantzos, N., & Nomoto, K. 1995, A&A, 298, 517
Rayet, M., Arnould, M., & Prantzos, N. 1990, A&A, 227, 271
Roberts, L. F., Woosley, S. E., & Hoffman, R. D. 2010, ApJ, 722, 954
Rogers, F. J., Swenson, F. J., & Iglesias, C. A. 1996, ApJ, 456, 902
Rosales, P., Aguilera, E. F., Martinez-Quiroz, E., et al. 2003, RMxFS, 49, 88
Siess, L., Goriely, S., & Langer, N. 2004, A&A, 415, 1089
Spillane, T., Raiola, F., Rolfs, C., et al. 2007, PhRvL, 98, 122501
Strieder, F. 2010, JPhCS, 202, 012025
Suijs, M. P. L., Langer, N., Poelarends, A.-J., et al. 2008, A&A, 481, L87
The, L.-S., El Eid, M. F., & Meyer, B. S. 2007, ApJ, 655, 1058
Thielemann, F. K., & Arnett, W. D. 1985, ApJ, 295, 604
Timmes, F. X., Woosley, S. E., Hartmann, D. H., et al. 1995a, ApJ, 449, 204
Timmes, F. X., Woosley, S. E., & Weaver, T. A. 1995b, ApJS, 98, 617
Tinsley, B. M. 1980, FCPh, 5, 287
Travaglio, C., Gallino, R., Arnone, E., et al. 2004, ApJ, 601, 864
Travaglio, C., Röpke, F. K., Gallino, R., & Hillebrandt, W. 2011, ApJ, 739, 93
Truran, J. W., Cowan, J. J., Pilachowski, C. A., & Sneden, C. 2002, PASP, 114, 1293
Vanhoy, J. R., Bilpuch, E. G., Westerfeldt, C. R., & Mitchell, G. E. 1987, PhRvC, 36, 920
Vázquez, G. A., Leitherer, C., Schaerer, D., Meynet, G., & Maeder, A. 2007, ApJ, 663, 995
Vink, J. S., de Koter, A., & Lamers, H. J. G. L. M. 2001, A&A, 369, 574
Woosley, S. E., Heger, A., & Weaver, T. A. 2002, RvMP, 74, 1015
Woosley, S. E., & Hoffman, R. D. 1992, ApJ, 395, 202
Woosley, S. E., & Howard, W. M. 1978, ApJS, 36, 285
Woosley, S. E., & Weaver, T. A. 1995, ApJS, 101, 181
Zickefoose, J. 2011, PhD thesis, Univ. Connecticut
Zickefoose, J., Schweitzer, J., Spillane, T., et al. 2011, in Nuclei in the Cosmos XI (Trieste: SISSA), PoS (NIC XI) 019